POLITECNICO DI TORINO
Repository ISTITUZIONALE

Development, verification and experimental validation of a 3D numerical model for tubular solar receivers equipped with Raschig Ring porous inserts

(Article begins on next page)
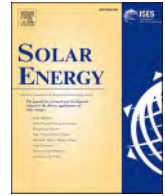
15 May 2024

Development, verification and experimental validation of a 3D numerical model for tubular solar receivers equipped with Raschig Ring porous inserts

Hossein Ebadi [a,*], Antonio Cammi [b], Eleonora Gajetti [a], Laura Savoldi [a]

[a] *MAHTEP Group, Dipartimento Energia "Galileo Ferraris" (DENERG), Politecnico di Torino, Italy*
[b] *Department of Energy, Politecnico di Milano, Italy*

A B S T R A C T

This study presents a numerical investigation of gaseous tubular absorbers used in a solar furnace and introduces a 3D model to simulate porous inserts with random packing of metallic Raschig Rings (RR) at pore-scale. A comprehensive verification and validation process was conducted based on the experimental data obtained at Plataforma Solar de Almeria (SF60). The evaluations were carried out on three samples, including a smooth pipe (SP) and two enhanced pipes (20RR and 40RR) with 20 mm and 40 mm RR inserts. The effects of several influential parameters, such as the fluid turbulence model, the effective thermal conductivity of the porous material, and the randomness of the RR in the porous structure, were studied to assess the accuracy and repeatability of the model in predicting thermal and fluidic characteristics of air inside the absorber pipes under different working conditions. A detailed thermo-hydraulic analysis revealed an irregular flow pattern inside the porous zone, while the air recirculation at the porous entrance and exit provides an uneven pressure drop distribution in the azimuthal direction. Moreover, fluid turbulence is enhanced downstream of the porous insert thanks to several stream jets formed by uneven flow discharge at the insert outlet face, which improves heat transfer in that area. The analyses demonstrated a significant improvement in heat transfer, with a maximum enhancement factor of 10–15 than the smooth tube. Additionally, in the evaluation of thermo-hydraulic performance, the enhanced absorbers exhibit Performance Evaluation Criteria up to 2, compared to the tube without RR inserts.

1. Introduction

The application of porous materials in energy conversion systems has been an important issue in recent years, owing to the need for designing efficient renewable energy systems. In principle, most porous materials provide a very large surface area, large pore volume, and tunable pore size and shape, which contributes to their exclusive use in solar energy conversion and storage applications [1]. Although the integration of porous materials with solar systems is a simple modification and does not require external energy for a positive impact on heat transfer, care must be exercised for the negative effects on the pressure drop and pumping power [2]. As a result, the proper utilization of various porous structures suitable for different solar systems has been a key factor aimed by scientists within the experimental and numerical works in the academic environment.

Solar receivers are the most studied porous application in solar systems while the literature also includes some examples such as porous material combined with solar chimneys [3], PVT [4], ponds [5], stills [6], and thermal storage units [7,8]. In this regard, low-temperature solar collectors have been investigated by many researchers where a number of porous materials have been proposed. Singh [9] integrated a porous serpentine wavy wire-mesh packed bed with a solar flat-plate air heater, conducting experimental and numerical studies. After the optimization process, it was reported that the wavy wire-mesh structure promotes fluid mixing at the trough and crest regimes, improving convective heat transfer. Continuing this approach, he later conducted a numerical study [10], investigating the effects of the fractional porous interface to meet the optimum measures of material cost and pumping power. In an experimental attempt, Khatri et al. [11] proposed an arched solar absorber enhanced with cylindrical porous wire-mesh aluminum fins. Results indicated that, although the arch design improves the thermal efficiencies due to the higher air turbulence and vortex generation, the addition of porous fins brings > 30 % to the thermal efficiency. Xiong et al. [12] proved the synergy between the nano-based thermal fluids and porous insert for performance augmentation in flat plate

---

* Corresponding author.
 E-mail address: hossein.ebadi@polito.it (H. Ebadi).

Nomenclature

Abbreviations

CFD	Computational Fluid Dynamic
CSP	Concentrating Solar Power
DEM	Discrete Element Method
EWT	Enhanced-Wall-Treatment
IR	Infrared
PEC	Performance Evaluation Criterion
PSA	Plataforma Solar de Almeria
PTC	Parabolic Trough Collector
PVT	Photovoltaic Thermal
RBD	Rigid Body Dynamics
RR	Raschig Ring
SP	Smooth Pipe
TC	Thermocouple
TPMS	Triply Periodic Minimal Surface

Greek symbols

α	absorption
β	viscous resistance coefficient (m^{-2})
γ	coefficient
Δh_i	average size of the i-th grid
Δp	pressure drop (Pa)
ϵ	emissivity
ε	turbulent dissipation rate
θ	incident angle
κ	turbulent kinetic energy (m^2/s^2)
λ	computed order of convergence
$\mathscr{L}$	least squares function
μ	dynamic viscosity (Pa.s)
ρ	fluid density (kg/m^3)
σ	Stefan–Boltzmann constant
σ_x	standard deviations in x direction
σ_y	standard deviations in y direction
φ	solar flux (W/m^2)
Φ_∞	extrapolated value
ω	specific dissipation rate of the turbulent kinetic energy (s^{-1})

Symbols

A	area (m^2)
C	inertial resistance coefficient (m^{-1})
Cp	specific heat capacity (J/kg/K)
D	diameter (m)
E	heat flux (W/m^2)
er	relative error
ETC	Effective Thermal Conductivity (W/m/K)
f	friction factor
h	heat transfer coefficient ($W/m^2/K$)
k	thermal conductivity (W/m/K)
L	length (m)
m	mass flow rate (kg/s)
N	cell number
Nu	Nusselt number
p	pressure (Pa)
Q	thermal energy (J)
r_{21}	ratio between the cell size of two grids
Re	Reynolds number
S	surface area (m^2)
T	temperature (K)
u	uncertainty
V	total volume of the model (m^3)
v	velocity magnitude (m/s)
x, y, z	coordinate system

Subscripts

amb	ambient
abs	absorbed
ave	average
c	cross section
con	concentrated
conv	convection
i	inlet
f	fluid
focus	concentrated solar flux
l	loss
m	mean
num	numerical
o	outlet
p	pipe
pi	pipe internal side
po	pipe outer side
peak	peak flux
rad	radiation
S	solar
sky	sky
u	useful
w	wind

collectors. Anirudh and Dhinakaran [13] numerically investigated the effects of porous block intermittency on the performance of a solar flat plate collector, showing that using a lower number of blocks with lesser height results in better thermal performances. In another work, Fallah Jouybari and Lundstrom [14] considered a thin layer of Aluminum oxide (Al$_2$O$_3$) ceramic as the cover below the absorber plate. This configuration led to the turbulence formation at the porous-fluid interface, which increases the heat transfer rate from the absorber and avoids hotspots due to no entrapped eddies creation over the absorber plate. Numerical analyses revealed that the maximum thermal enhancement is 5 times greater than those obtained without the porous, while the pressure drop rises only 2 times with the porous insert. The other porous materials and structures such as steel chips [15], copper foam [16,17], ironic packed bed [18], aluminum fibers [19], triply periodic minimal surface (TPMS) [20], and elastic porous winglet [21] have also shown promising improvements in solar low-temperature applications.

The application of porous inserts for medium and high-temperature solar absorbers has also piqued the interest of some researchers. However, the non-uniformity of the heat flux is a major factor in heat transfer improvement as the heat propagation inside the porous medium is non-uniform and complex, which requires more explanations and clarifications [2]. Therefore, Kumar and Reddy [22] presented a 3D numerical model to assess a stainless steel porous disc receiver for parabolic trough collectors (PTS). The concept of porous discs was tested experimentally in a 15 m^2 solar PTC by Reddy et al. [23], revealing lower heat losses compared to the smooth design. Later, scientists [24] proved that decreasing the inner diameters of the porous rings or reducing the distance between them increases the heat transfer coefficient. Zhang Jing et al. [25] developed an optimization method based on CFD and a genetic algorithm to enhance a PTC with several porous inserts. Results suggested that if high conductive materials such as Cu, AL, and SiC are employed as the porous medium, the obtained solar-to-thermal energy conversion efficiency reaches almost 70 %, using the optimized receiver. In another study [26], the potential of the combination between nanofluids and annular porous inserts in a PTC receiver was assessed numerically. It was concluded that the effects of the porous insert on the HTF performance working at Reynolds numbers ranging from 5×10^5 to 15×10^5 are higher than at the other flow rates. In a similar study

conducted by Siavashi et al. [27], no-porous, half-porous, and full-porous cases were compared for a PTC receiver. Assuming the utilization of an open-cell aluminum metal foam structure with constant and uniform porosity of 0.9, results showed that as the Grashof number decreases or Darcy number increases, the Performance Evaluation Criteria (PEC) for a full-porous design is 10 times higher than that of the half-porous case. Aryan et al. [28] proposed the integration of some porous lines with a rotating PTC receiver that works with nanofluids. Using this configuration, the rotational movement of the receiver avoids the local temperature rise at the bottom of the absorber, while the presence of porous media improves the flow mixing and enhances the thermal performance of the tube. The reported numerical data asserted a 15–40 % increase in thermal efficiency solely due to the porous integration. Samiezadeh et al. [29] performed a CFD simulation of a finned PTC receiver, in which the inner wall is enveloped in an aluminum porous medium with a porosity of 0.5. The application of $Cu-Al_2O_3$-synthetic oil with three longitudinal fins at the bottom side of the tube resulted in a 12 % increase in thermal efficiency and a 5 % growth of friction factor compared to the plain design. In an attempt by Helmi et al. [30], a range of porous fin materials was tested for energy storage potentials in a rotary PTC absorber, operating with nanoparticles. Considering the copper, aluminum, bronze, and steel foam materials as the annular porous medium through a numerical study, the copper foam was found to have the highest hydro-thermal performance, due to the higher energy absorption and less exergy destruction. The rotation further enhances the improving effects of the porous material as the centrifugal force circulates the nanofluids. Moreover, the recommended operating conditions were reported to have ∼ 15 % more energy efficiency. The application of an open-cell copper porous medium as a volume absorber in a direct absorption PTC was also conceptualized by Heyhat and Zahi Khatar [31] during an experimental campaign. Jamal-Abad et al. [32] used copper foam in a small-scale PTC receiver, where the overall loss coefficient was reduced by 45 %.

As the literature survey shows, the optimum integration of porous inserts with solar receivers depends on several porous parameters such as porosity, thermal conductivity, inertia, and viscous coefficients. Therefore, as new porous materials emerge for application in solar absorbers, their hydraulic and thermal characteristics must be well-defined for further optimizations. This study aims to clarify the hydro-thermal features of a novel and emerging porous material made of metallic Raschig Rings (RR) for application in tubular solar absorbers.

Raschig Rings are versatile components that have been used for decades in various chemical [33] and industrial [34] practices for different purposes. Having a central hollow channel makes these particles excellent candidates for use as the packed bed material, especially in applications where high mixing flow is important. One of the fundamental works on RR packed-beds was conducted by Rao and Gnielinski [35], measuring the mass transfer coefficients through an experimental study. Also, the characteristics of solid–fluid mass transfer under various RR packed beds have been addressed in [36–38]. As the particle dispersion is completely random in RR packed beds, the statistical variation of RR was also the subject of some research. Niegodajew and Marek [39] used a sequential algorithm to check the limits for reproducibility of the results obtained within the experiments and simulations. They found that, as far as the orientation distribution is concerned, results are strongly affected by sample size. Vice versa, in the case of porosity profiles, which describe the local pore variation within the medium quantitatively, the sample size has no significant influences. An experimental trial on RR was conducted by Samantaray et al. [40], exploring the effects of geometrical parameters on the terminal velocity and drag coefficient of a single ring in a vertical and inclined channel. Results revealed higher drag forces on RR than the solid cylindrical particles. Yang and Du [41] combined the CFD and Discrete Element Method (DEM) to develop a macrostructure of a packed-bed RR for optimization and study of the reaction conditions in a photocatalyst. Marek [42] modeled gas flow through a packed bed of RR, using the

control volume method with a simple Cartesian structured grid. In their work, an immersed boundary method (IBM) was used to develop the packed bed with arbitrary RR where the application of a classical Navier-Stokes equations solver based on the projection method leads to the model development. However, the limitation of this technique allows its use only for fundamental fluid analysis and not for heat transfer problems, in which unstructured grids with local adaptation are necessary. Moghaddam et al. [43] used the sequential Rigid Body Dynamics (RBD) method and Computational Fluid Dynamics (CFD) simulation to provide the hydrodynamic behavior of airflow through a packed-bed RR. Developing a 3D numerical setup with a Realizable k-ε model and an Enhanced-Wall-Treatment (EWT), the obtained numerical results were later validated against experiments. Results demonstrated a significant velocity inhomogeneity along the azimuthal and axial directions of the channel, where the orientation of RRs has a salient role in forming the local flow fields. In another study, Moghaddam et al. [44] assessed the heat transfer from the wall to the bed of RR and proved that fluctuations in local temperature are completely discarded by azimuthal averaging of 3D temperature fields over the bed volume.

As discussed in the earlier works, the pore structure of RR packed beds offers excellent potential for heat dissipation applications with reduced pressure drop compared to other porous structures [44–46]. In this regard, Allio et al. [47], analyzed a porous medium made of metallic mm-size RR as a high-efficiency cooling method for Gyrotron Resonance Cavities. Comparing the measured hydraulic behavior to an identical sample with microchannels revealed that the RR porous medium results in a two-fold lower pressure drop when water is used as the coolant. The validity of using DEM simulations for geometry development was also confirmed with good agreement between CFD and experimental data. Later, Savoldi et al. [48] introduced this technology to solar applications,[1] testing a gaseous planar mockup in a solar furnace and developing a 3D model for the absorber through DEM integration. Based on the experimental and numerical data, it was shown that the insertion of RR porous medium below the heated side allows the maximum surface temperature to decrease significantly, with a nearly 5 times higher Nu number, compared to a plain channel using the same envelope. As a follow-up of that research line, an air-based tubular absorber was then tested experimentally with the insert of RR porous media to check the applicability of such technology for various solar absorbers[2] [49]. The obtained results demonstrated that RRs are able to increase the energy and exergy efficiencies by respectively ∼ 30–50 % and ∼ 60–75 %, depending on the length of the porous medium used in the absorber. This study aims to build upon the previous work [49], incorporating the numerical investigation to provide robust models in simulating the RR porous media in pore scales (micro-size) and elaborate on the effects of the porous length on the performance augmentation in tubular solar absorbers. Moreover, the presented analyses provide some new insights into the heat transfer mechanism through the metallic RR matrix formed as a packed medium, exploring the impacts of several influential parameters on the numerical simulations. The selected parameters are among those that despite their effectiveness, have not been addressed in the previous works and still need more information, using a precise and extended validation process. Therefore, the novelty of the proposed work lies in the methodology, ranging from the development of a new and general model for packed-bed porous materials to a comprehensive validation process in which the effects of several modeling parameters are investigated separately against the experimental results. To the best of the authors' knowledge, there was not any similar study for packed-bed porous materials, proposing a 3D CFD model in simulating the heat transfer phenomenon in the solar energy context and at the pore

scale, recognizing the possible affecting parameters, and providing detailed fluidic and thermal analysis. Moreover, the comparison between the different turbulence models has not been ever investigated thoroughly for such materials (RR porous media) and this study provides a precise evaluation of each model performance in terms of their local effects on the temperature distribution along the absorbers. The structure of the current paper can be divided into two main parts. In the first section, a CFD-based numerical model is developed, verified, and thoroughly validated against the experimental data, where the effects of different numerical parameters such as RR randomness, porous Effective Thermal Conductivity (ETC), and fluid turbulence models are examined and optimized during the validation process. Then, the thermo-hydraulic behaviors of the samples are discussed and compared in detail, considering the changes in friction factors, Nu numbers, and performance evaluation criteria.

2. Material and methods

2.1. Solar absorber

Fig. 1a and b show the concept of the RR porous insert for a conventional tube, in which the porous block is installed and brazed inside to enhance the heat transfer rate, as tested in [49]. The structure of the porous medium was formed using numerous RR elements made of copper, coated with an Au alloy, and brazed together with a porosity of 78.8 %, the same material used in previous works [47,48]. The exact manufacturing procedure is a company confidentiality, but its cost is

probably higher than other traditional porous inserts, mostly because of the choice of the materials [50]. However, this type of RR matrix leads to a great increase in the heat transfer compared to other materials. Moreover, to increase the solar absorption and improve the durability of the samples in a high-temperature process, black PYROMARK 2500 coating was applied to the samples through a specific curing time and procedure [51]. The dimension of the absorber was selected based on the experimental work, which was conducted at the Solar Furnace (SF60) located at Plataforma Solar de Almeria (PSA), Spain. Since the study was focused on the thermal augmentation in RR-based tubular absorbers which could be used later as an element of billboard receivers, the tests and analyses conducted are devoted to the tube virtually located in the middle of the billboard (the one with the highest heat load), following the procedures addressed in [48,52]. The reported results for the smooth pipe (SP) design and the two modified tubes with 20 mm (20RR) and 40 mm (40RR) RR inserts are used for the validation of numerical simulations in section 3. Table 1 provides the specifications of the absorber and the test facility.

2.2. Experimental tests and measurements

As documented in [49], the experimental campaign was conducted in June 2022 as part of the SFERA-III Transnational Access Activities. It is noteworthy to mention that prior to the thermal tests, several hydraulic tests were performed on the two modified solar absorbers (20RR and 40RR), testing a wide range of airflow rates (200 NL/min – 800 NL/min) in the absence of solar radiation, as indicated in Table 2.
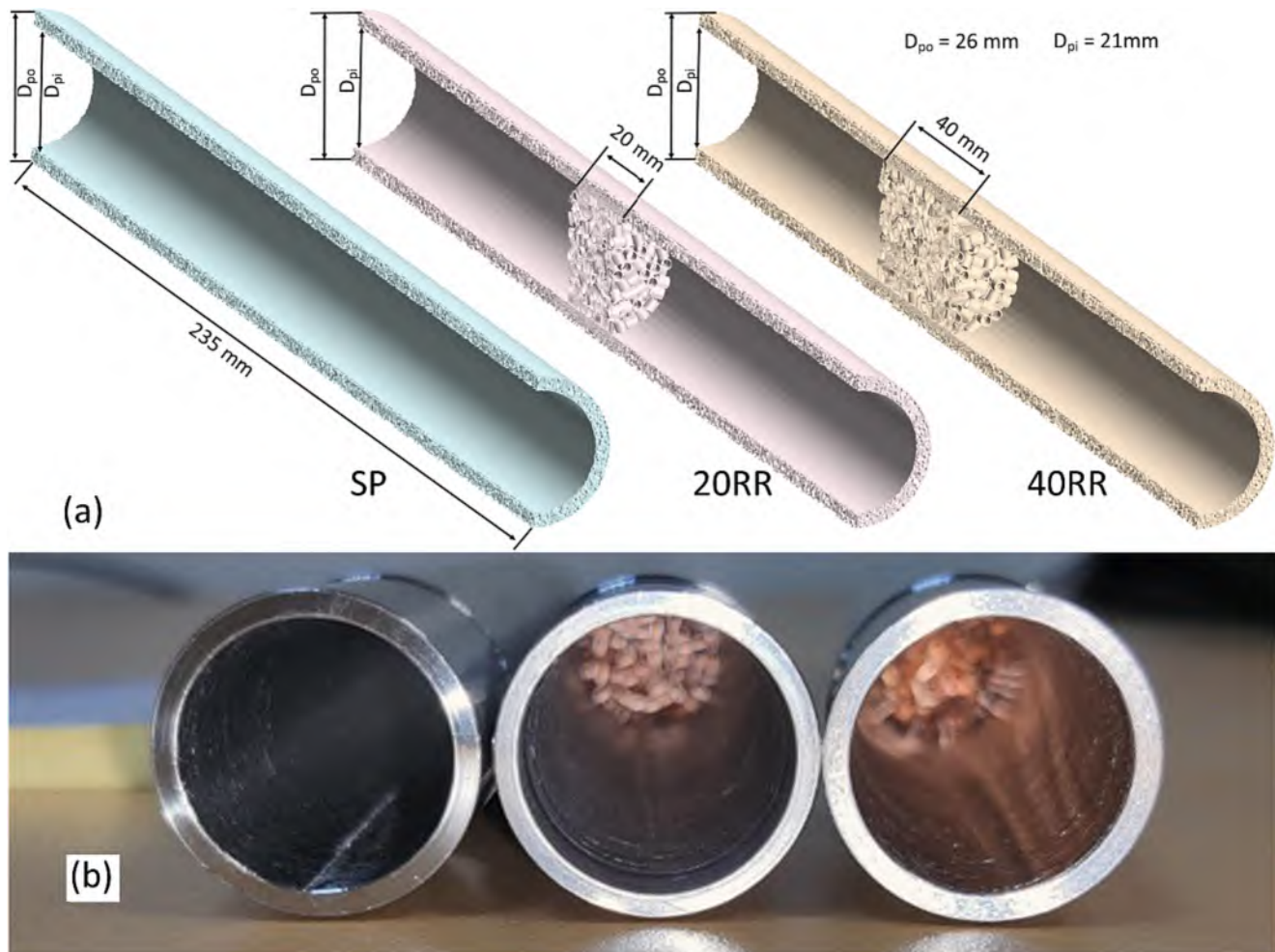

Fig. 1. (a) Schematics (section cut view) of the 3 different samples, including SP, 20RR, and 40RR, (b) photograph of the samples after fabrication.

Table 1
Specification of the solar absorber and test facility.

Specification	Value/Dimension
Tube inner diameter (D_{pi})	21 mm
Tube outer diameter (D_{po})	26 mm
Tube length (L)	235 mm
Tube material	316L stainless-steel
Tube coating	PYROMARK 2500
Solar furnace nominal power	80 kW
Maximum solar peak flux	6.7 MW/m^2
Heliostat area	130 m^2
Parabolic dish aperture	108 m^2
Working pressure	10 bar

Table 2
Experimental specifications of the hydraulic tests.

Nominal Airflow rate (NL/min)	Inlet pressure (bar)	
	20RR	40RR
200	9.5	9.5
300	9.3	9.4
400	9.2	9.2
500	9.1	9.1
600	8.9	8.9
700	8.7	8.8
800	8.6	8.6

Subsequently, the samples were heated and monitored under different operating parameters, such as the airflow rate (30, 40, and 50 NL/min) and solar peak heat flux (50, 100, 200 kW/m^2), resulting in a total of 27 experimental tests. The experimental test rig comprised several measuring tools as shown in Fig. 2a, including an F-203AV mass flow-meter with an accuracy of 2 % for gas fluids, a water-cooled asymptotic circular foil calorimeter with an accuracy of 3 % to measure the amplitude of the solar peak flux, and a pressure transmitter (Model S-10) with a nonlinearity of 0.2 %. Also, a PD-type differential pressure sensor was used for the measurement of the pressure difference across the test section, including some joints and connections, with an accuracy of ± 2.40 % + 5 mbar. Moreover, two parallel methods were employed to measure the absorber temperature, providing a detailed temperature profile along the tube walls. First, an infrared (IR) camera with a 2 % uncertainty was placed on the front side of the samples to capture thermal images from the heated side and later post-processed to record the tube hotspot temperatures. Second, a set of K-type thermocouples with a Class Tolerance I (±1.5 °C in the range of −40 °C to 375 °C and 0.004×|T|, where T is the measured temperature in Celsius (°C), in the range of 375–1000 °C) were mounted and welded on the backside of the tube samples, ensuring good contact with the wall to provide local temperature data. Fig. 2b-d show the location of the IR camera and wall thermocouples with respect to the SP and RR samples. Additionally, two more thermocouples were inserted in the fluid channel, one upstream and one downstream to measure the air inlet and outlet temperatures. Table 3 includes the details of the tests performed during the experimental campaign.

One of the important factors that must be considered during the wall temperature measurement was the quasi-steady state that is reached on all the components [48,49]. The reason for not achieving a fully steady state condition is the nature of the coming solar radiation, which increases before the solar noon and decreases after. Thus, the temperature readings continued for at least 2 min after the quasi-steady state was reached, and thermal images were also captured from the front side of the samples. Consequently, the experimental errors were calculated for the thermocouples, accounting for the ± 1.5 K intrinsic reading uncertainty of the thermocouples (which was counted twice, as it represents the temperature difference between two thermocouples) plus the standard deviation calculated from the two-minutes or longer "quasi-steady-

state" period. Moreover, concerning the hotspot temperature measurements with the IR camera, the experimental error was computed with the accumulation effects of the standard deviations due to the absorber emissivity (the two values used during the experiments) as well as a 2 % uncertainty in the thermographs.

Since the solar flux was to be limited to only one tube, the reflected flux was regulated within a slot (160 mm height and 30 mm width) created on a protective shield as shown in Fig. 3a. Therefore, during the heating stage, the redundant solar flux was covered by the shield to protect the test facility from excessive exposures (Fig. 3b). As a result, the restricted solar flux was used in the simulations to develop and validate an accurate thermal model.

2.3. Numerical investigation

The numerical works conducted for this study can be divided into two integrated parts. Firstly, a transient DEM model was used to generate the RR geometries. Then, a robust thermal model was developed, verified, and validated through CFD analysis on the SP, 20RR, and 40RR samples. During this phase, the validation process was designed to investigate the accuracy of the thermal model, the geometry generation of the RR porous medium, as well as the sensitivity of effective thermal conductivity of the RR porous medium and the RR particles randomness on the absorber wall temperatures. The numerical simulations used during the process are developed using the commercial software Star CCM +.

2.3.1. Development of porous media structure

In the literature review section, it was mentioned that one of the methods for generating the random packed-bed RR is DEM modeling [48]. As a result, a time-dependent discrete element model was used to model the falling of RR particles into a control volume under the influence of gravity. A Lagrangian multiphase model was implemented where, in the multiphase interaction, the DEM phase interaction was set as cylinder for both the first and second phase and a linear spring model with a constant stiffness of 10000.0 N/m was used. The void space between the DEM particles was considered as air with a 0 velocity and 0 reference pressure. The simulations were conducted in a laminar regime, covering a total physical time of 10 s with a time step of 0.001 s. The generation of the RR porous medium began by defining the volume of the bed and then running the DEM simulation. At each step, a certain number of solid cylindrical particles were injected. The particles were randomly injected in a specific number based on the desired target porosity, with angular and axial velocities both set to 0. The procedure continued until the required number of particles was achieved, and they settled in the bed. Finally, by extracting the position of each particle, the solid cylinders were replaced by hollow cylinders to create the actual porous geometry with RR as the particle component. Fig. 4 illustrates the process of generating the 40RR porous block using the DEM method.

2.3.2. Model and simulation setup

In order to validate the numerical models against the experiments, it was necessary to model not only the sample but also the connectors leading to the locations where pressure and fluid temperature sensors were situated. Therefore, the effects of the entrance and existing sections are accounted for and the solution domain was extended beyond the original sample length. In this context, the boundary of the control volume encompassed an inlet section, the tube sample, and an outlet section. The computational domain included both the solid and fluid regions of the irradiated samples and the RR porous medium inside RR models. A steady-state, 3D conjugate heat transfer model was applied to all regions. Regarding the boundary conditions, a velocity inlet boundary condition was defined on the fluid inlet face, while a pressure outlet (with pressure gauge p = 0 Pa) condition was set for the outlet face. The concentrated solar flux was simulated through the field functions applied to the irradiated side of the sample (Fig. 5a). The boundaries of
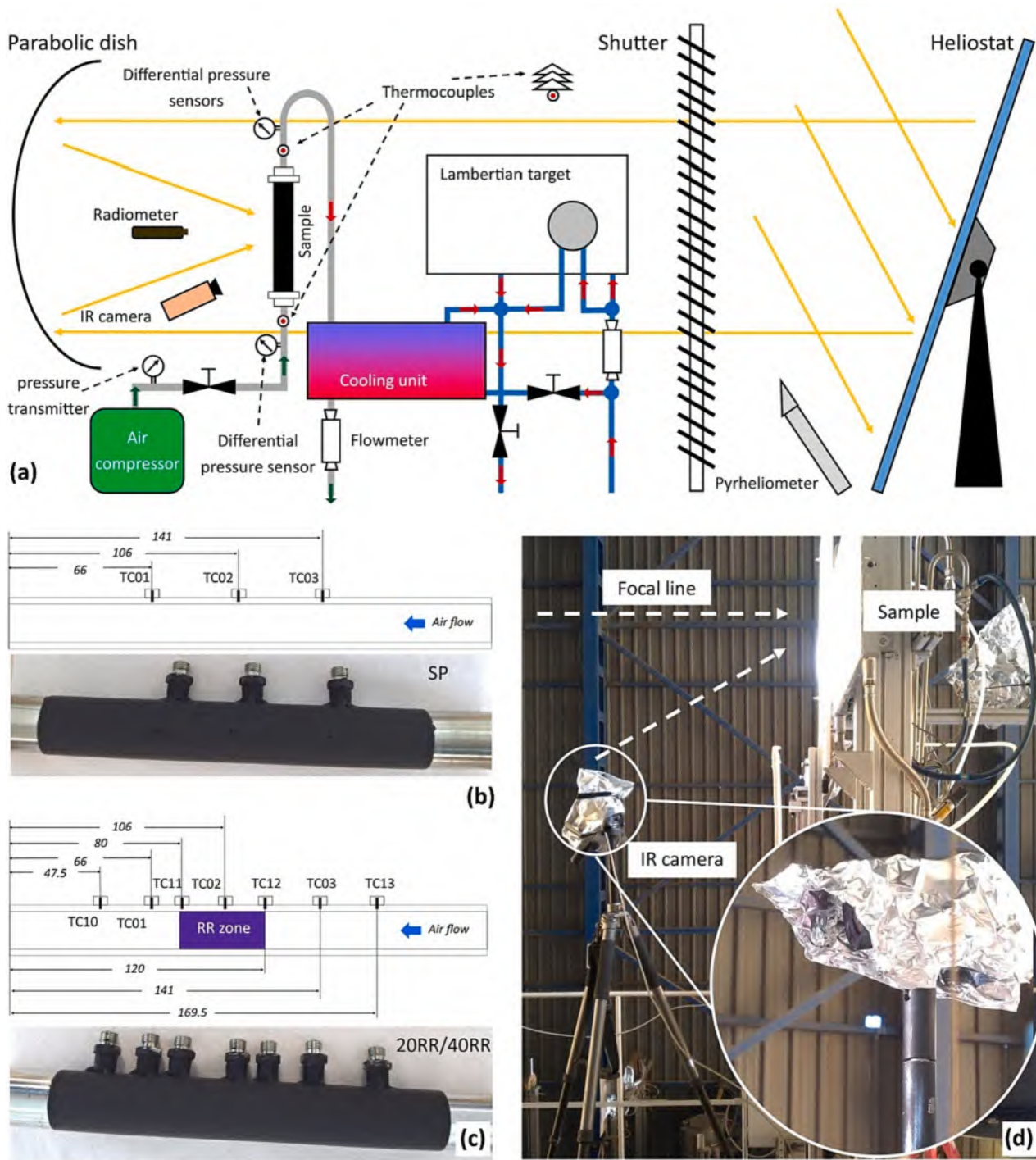
Fig. 2. Details of the test setup used during the experimental campaign; (a) the layout of the test rig (b) thermocouples mounted on SP sample (dimensions are in mm), (c) thermocouples mounted on 20RR and 40RR samples (dimensions are in mm), (d) the lR camera employed for temperature recording from the heated part of the samples.

the two inlet and outlet sections were considered as adiabatic as the conduction has a negligible role in total heat loss from the receiver [52]. Furthermore, a no-slip boundary condition was imposed at the walls, and the inlet air and ambient temperatures were set in accordance with experimental observations (Table 3). Fig. 5b-d depicts the three simulated absorbers with the relative dimensions as used within the simulation study.

According to the examined airflow range ($4000 < \mathrm{Re} < 8000$), it was determined that the fluid flow regime throughout the entire computational domain was turbulent. As often justified in the literature [47], the

$k - \omega \, SST$ (Menter) turbulence model with an all-y + wall treatment was selected as the reference model for reproducing the fluid flow in the packed RR particles. The rationale behind the choice is due to the improved performance of the $k - \omega$ model in modeling the boundary layers under adverse pressure gradients, which is pronounced in the presence of RRs [48]. Also, its higher ability than the $k - \varepsilon$ model for predicting turbulence near walls and separated flows, supports this selection. Moreover, in the work conducted by Allio et al. [47], the suitability of the $k - \omega \, SST$ over the realizable $k - \varepsilon$ model was demonstrated in predicting the hydraulic behavior of a flow within the RR porous

Table 3

Details of the experimental tests. The test ID is given for each test by the concatenation of the targeted heat flux value with the flow rate value (for example, 5030 indicates the test with 50 kW/m2 peak heat flux and 30 NL/min airflow rate).

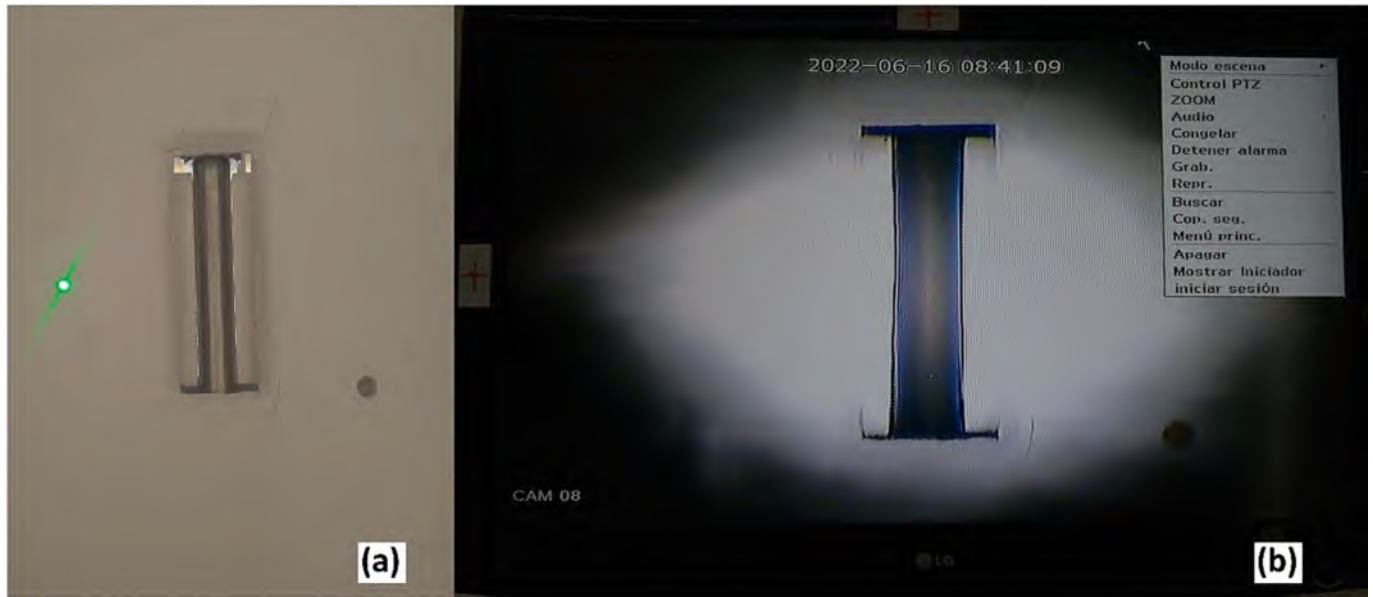| Sample	Test ID	Peak heat flux (kW/m^2)	Nominal Airflow rate (NL/min)	Ambient temperature (^{o}C)	Inlet temperature (^{o}C)	Inlet pressure (bar)
SP	5030	49.5	30	28.6	27.3	9.9
	5040	48.7	40	29.8	28.2	9.2
	5050	48.2	50	30.4	28.5	9.6
	10,030	101.2	30	31.1	29.4	9.8
	10,040	98.4	40	32.0	30.5	9.8
	10,050	101.1	50	33.2	31.6	9.6
	20,030	196.9	30	28.5	27.1	9.3
	20,040	199.2	40	34.5	32.6	10.0
	20,050	202.4	50	27.4	25.7	9.2
20RR	5030	48.8	30	30.9	29.8	9.3
	5040	50.2	40	33.9	32.3	10.8
	5050	50.9	50	33.4	31.9	10.2
	10,030	97.2	30	34.5	33.0	10.0
	10,040	101.4	40	35.3	33.8	9.8
	10,050	102.9	50	36.0	34.7	10.2
	20,030	198.7	30	36.5	34.9	9.7
	20,040	194.1	40	38.7	37.0	9.5
	20,050	200.5	50	39.3	37.5	9.7
40RR	5030	49.9	30	32.5	31.4	10.3
	5040	46.7	40	34.5	33.5	9.37
	5050	47.0	50	35.5	34.2	9.6
	10,030	101.7	30	36.4	35.2	9.7
	10,040	104.1	40	37.0	35.61	9.6
	10,050	96.0	50	37.6	36.1	9.5
	20,030	199.0	30	38.8	37.3	9.7
	20,040	200.2	40	39.5	37.7	10.2
	20,050	198.5	50	40.1	38.0	10.0

Fig. 3. Photographs of the sample and the protective shield; (a) before the heating, (b) during the heating.

media. However, in the interest of selecting an appropriate RANS turbulence model, this study also aims to evaluate the potential of the lag elliptic blending (lagEB) $k-\varepsilon$ model in simulating the separated flow inside the RR region and considers it as an alternative to the $k-\omega\,SST$ (Menter) turbulence model. The reason for this comparison stems from the fact that the treatment of turbulence in the bulk flow for the two models is somewhat similar to the $k-\varepsilon$ model, while their near-wall turbulence treatment differs. In particular, the lag elliptic blending model incorporates additional terms to model the effects of anisotropy and offers good predictive capability for flows subjected to rotation or strong streamline curvatures [53].

One of the important factors in studying the RR porous medium is its

ETC, which remains unknown after the brazing process. As previously mentioned in another work [48], ETC is determined through a calibration process using numerical simulations. This process not only considers the conductivity of the copper alloy (RR material) and gold alloy (brazing material) but also accounts for the heat flow through contact points between the individual RRs. Therefore, this study aims to investigate various ETC values for RR and assess their impact on predicting tube wall temperatures. To achieve this, four thermal conductivity levels ranging from 500 (similar to that of the base material, which is copper) up to 3500 W/mK were examined and compared against the experimental data. These values were made as some sort of correction to compensate the contact surface from point contact (similar to the
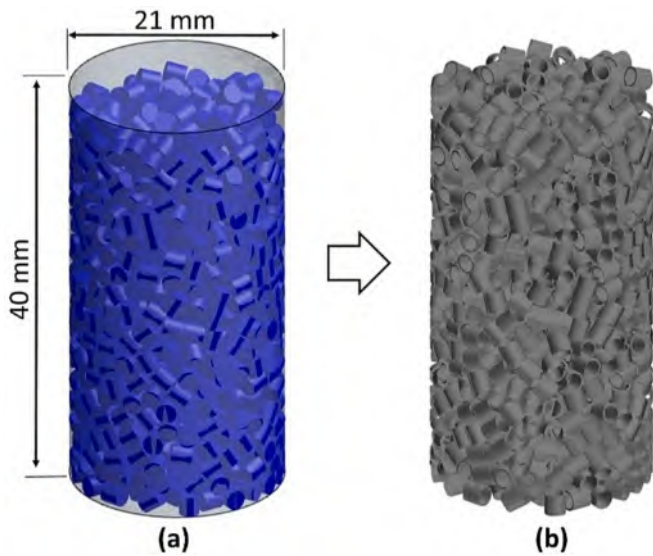
Fig. 4. Schematic of the DEM procedure for the RR matrix generation in a cylindrical sample, as also discussed in [47]; (a) DEM particles compact matrix, (b) definitive matrix after the replacement of the particles with RR.

simulation) to a wider contact due to the effect of the brazing (similar to the real samples). It is worth noting that an ETC value of 2000 W/mK is typically employed in the modeling of the gyrotron cavities where RR is typically used as heat sinks. This value takes into account the effect of the brazing material, which increases the contact points between rings and has been demonstrated to provide a global agreement between computed and measured performance of the device [54].

Moreover, upon the temperature reading from the tube wall, some random and local temperature peaks could appear due to the contacts between the RR particles and the tube wall, as shown in the previous

work [45]. This may influence the comparison between CFD and experimental data. To investigate the effects of such a phenomenon, the heat load position was changed by three other orientations, accounting for three more random distributions of the RRs within the tube. It is important to note that, for the sake of simplifying the validation process among the 27 different tests, these sensitivity investigations were performed only on the worst-case study (20030) with the highest solar load and the lowest airflow rate.

The other considerations and assumptions used in this study can be listed as the following:

- The thermal analysis in this work was performed using a segregated flow temperature model,
- The solid and fluid properties are temperature dependent,
- Solid temperature values used for the calculation of heat transfer coefficient are obtained, using the surface average report at the interface between the fluid and solid,
- Tube emissivity with the applied coating was set as a function of wall temperature defined in [55],
- The convection heat transfer coefficient for the loss through the absorber to the ambient (h_w) was set as 10 W/m^{2}K,
- All the input parameters, including peak heat flux, airflow rate, ambient temperature, air inlet temperature, and inlet pressure used for each test at the validation procedures were based on the values reported and measured during the experiments, as detailed in Table 3,
- Hotspot temperature measurements are obtained, using a temperature maximum report on the outer tube surface.

2.3.3. Grid study

In this research, a polyhedral-based meshing with a prismatic layer for fluid regions was employed to solve the equations. As shown in Fig. 6, custom controls were adopted to the boundary layer areas to refine the meshing with specific care, especially for the RR porous zone.
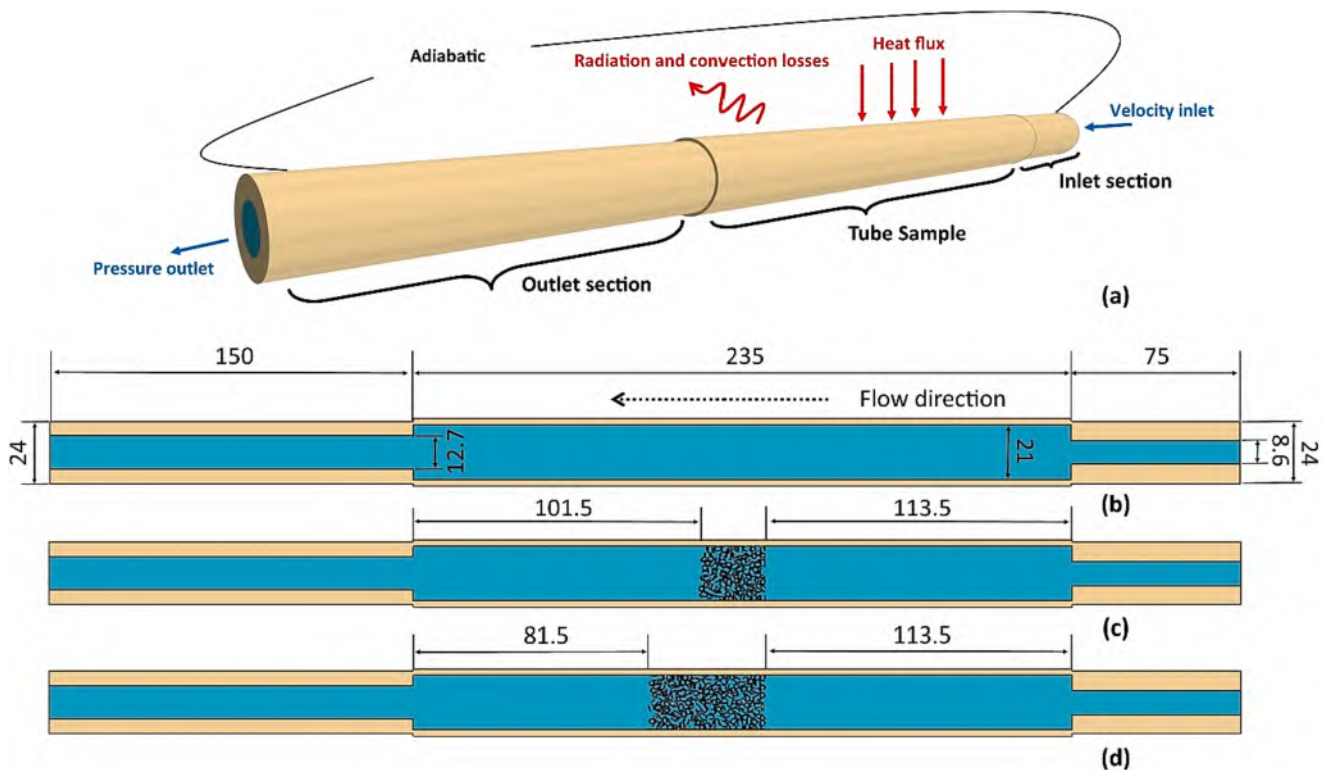

Fig. 5. (a) Boundary conditions applied on the full geometry, dimensions of (b) the SP model, (c) the 20RR sample, and (d) the 40RR sample, respectively (note that dimensions are in mm). Flow direction from right to left.
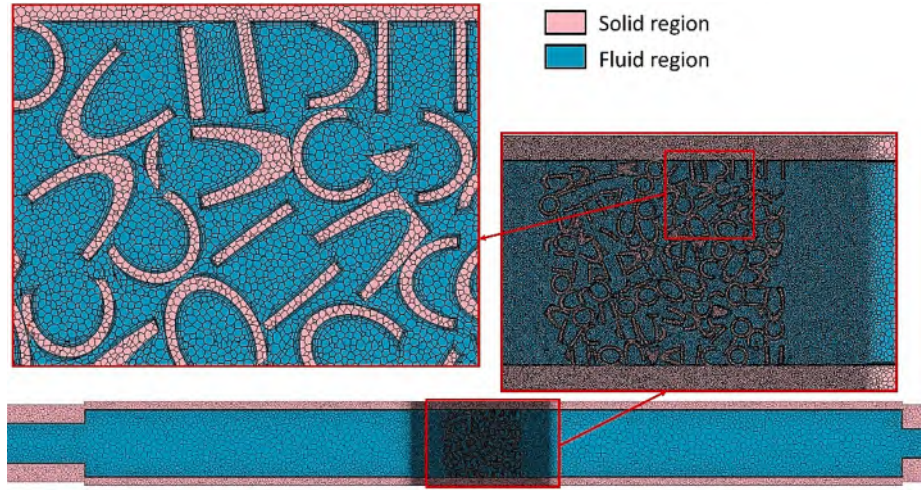
Fig. 6. Cross-sectional view of the mesh developed in this study for RR sample with a custom control on the porous area.

While in the core area of the fluid, where the velocity and temperature gradients are smoother, cells become coarser and uniform along the length of the tube. To check the accuracy of the results related to the discretization error, two grid convergence studies were carried out: one for SP simulation and one for RR simulations. The refinement of the grid has been achieved by first giving a constant base cell size and increasing the base cell size until y + reached 1. Then, the number of prism layers was frozen, and the base cell size was decreased until convergence was achieved in the results. As a result, four different meshes were formed for each sample ranging from the very coarse mesh to the finest mesh, comparing the pressure drops and outlet temperatures (Table 4). The average cell size in the table was computed as $\sqrt[3]{V/N_{cell}}$ where V is the volume of the fluid in the case of Δp or the volume of the fluid and solid regions in case of ΔT_{mo}, and N_{cell} is the number of cells. Pressure drop has been computed on the whole fluid domain, and ΔT_{mo} is the difference between the mass flow average of the fluid temperature at the outlet and the inlet temperature. Concerning the SP, the entire tube region has been considered for the grid analysis of the outlet temperature, while for the 20RR sample, only the RR region was account. In Fig. 7, the RR region is highlighted in pink. The mass flow average of the fluid temperature T_m is computed as in Eq. (1).

$$T_m = \frac{\int_A \rho v C_p T dA_c}{\int_A \rho v C_p dA_c} \tag{1}$$

2.3.4. Assessment of the numerical errors

As already remarked in section 2.3.2, the number of experiments is extremely large. Therefore, the assessment of numerical errors was conducted exclusively on the worst-case scenario (20030), which featured the highest solar load and the lowest airflow rate, too.

In accordance with the ASME V&V 20–2009 Standard [56], numerical uncertainties were determined using the least squares approach.

Table 4
Details of the grid convergence results obtained for SP and 20RR samples.

Sample	Mesh No.	Average cell size (mm)		$\Delta p/\Delta p_{ref}$	$\Delta T_{mo}/\Delta T_{mo,ref}$
SP		*Fluid*	*Fluid & solid*		
	1	0.728	0.763	0.993	0.988
	2	0.593	0.629	0.997	0.993
	3	0.506	0.540	0.998	0.992
	Base	0.418	0.452	1	1
		Fluid	*RR region*		
20RR	1	0.272	0.130	0.968	1.002
	2	0.266	0.127	0.972	1.003
	3	0.253	0.122	0.980	1.004
	Base	0.220	0.104	1	1

This approach involves minimizing the least squares function $\mathscr{L}(\phi_\infty, \gamma, \lambda)$ as described in Eq. (2), to determine the extrapolated value ϕ_∞, the computed order of convergence λ and the coefficient γ. Here, Δh_i is the average size of the *i*-th grid and ϕ_i represents the relevant variable computed with the i-th mesh.

$$\mathscr{L}(\phi_\infty, \gamma, \lambda) = \sqrt{\sum_{i=1}^{4} \left(\phi_i - \left(\phi_\infty + \gamma \Delta h_i^\lambda\right)\right)^2} \tag{2}$$

The formulation of $\mathscr{L}(\phi_\infty, \gamma, \lambda)$ is based on the assumption that the deviation of any computed variable to the exact (extrapolated) value follows a power-law dependence on the average cell size, as depicted in Eq. (3).

$$\phi_i - \phi_\infty \approx \gamma \Delta h_i^\lambda \tag{3}$$

After minimizing $\mathscr{L}$, the numerical uncertainties u_{num} have been computed as in Eq. (4):

$$u_{num} = \frac{1.25}{1.15} \frac{er_{rel}^{21}}{r_{21}^\lambda - 1} \tag{4}$$

where er_{rel}^{21} is the relative error between values computed with the finest and the second finest grid, r_{21} is the ratio between cell numbers of the finest and the second finest grids. These coefficients are suggested by [55].

In Fig. 8, the pressure drop, the maximum solid temperature, and the outlet temperature have been plotted against the corresponding average cell sizes for the 20RR sample. Although the trends do not distinctly indicate an asymptotic value, the relative differences between the results are quite small. It should also be noted that the size of each RR is extremely small compared with the overall domain, which restricts the feasibility of employing either coarse or extremely fine cells in the RR region, due to accuracy or computational cost issues, respectively.

The numerical errors calculated in this manner are subsequently utilized in the subsequent work to provide error estimations for all the tested cases. This approach ensures a conservative assessment, as the considered worst-case scenario, featuring the highest pressure drop and heat flux, yields the largest numerical discretization errors.

On the other hand, the model of the smooth pipe exhibits a more convergent trend when refining the grid, as expected due to the straightforward geometry. Indeed, Fig. 9 depicts the thermal–hydraulic results of the SP computed using both $k - \omega SST$ and $k - \varepsilon$ LagEB turbulence models.
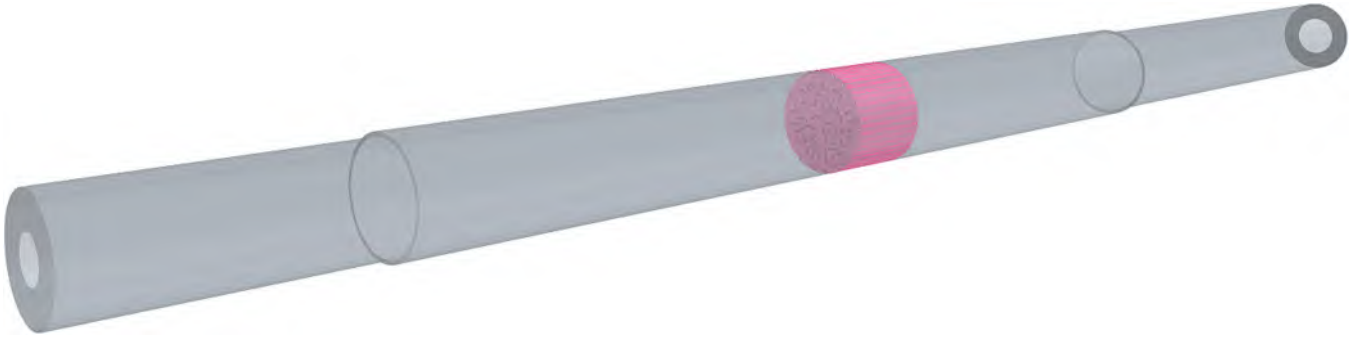
Fig. 7. 20RR pipe with the RR region emphasized.

2.3.5. Thermal modeling

This section outlines the theories and numerical assumptions employed in the development of the thermal model within the CFD simulations. According to [57], the spatial distribution of the solar flux in a solar furnace typically follows a Gaussian-shaped, rotationally symmetric with the peak in the center. However, in practical tests, various factors like the concentrator shape and shutter blades can influence its distribution. For simulation purposes, the concentrated solar flux imposed on the focus $E_{(S-focus)}$ was considered and calculated using Eq.5 as a function of the power along the tube perimeter [58].

$$E_{(S-focus)} = \iint \varphi_{peak} \times e^{-0.5\left[\left(\frac{x}{\sigma_x}\right)^2 + \left(\frac{y}{\sigma_y}\right)^2\right]} dxdy\cos\theta \tag{5}$$

where φ_{peak} is the maximum solar incident at the focal point ($\theta = 0$), σ_x and σ_y are standard deviations in x and y directions equal to 0.053 and 0.050 m respectively [49], and $\cos\theta$ reflects the projection flux on the curvature of the tube by accounting incident angle (θ).

The amount of heat absorbed by the solar receiver is a function of the tube absorptivity coefficient (α), which can be presented as Eq. (6).

$$E_{(S-abs)} = \alpha E_{(S-focus)} \tag{6}$$

The amount of the absorbed solar energy that is converted to the useful heat E_u can be defined as Eq. (7)

$$E_u = E_{(S-abs)} - E_l \tag{7}$$

where E_l is the total thermal power lost from the absorber to the ambient. This loss occurs primarily in the forms of convection $E_{l,\,con}$ and radiation $E_{l,\,rad}$ losses, while the conduction losses to the experimental structure are neglected.

$$E_{l,\,conv} = h_w\left(T_p - T_{amb}\right) \tag{8}$$

$$E_{l,\,rad} = \sigma\epsilon_p\left(T_p^4 - T_{sky}^4\right) \tag{9}$$

where T_{sky} denotes the surface temperature of the sun and is usually predicated as 5762 K.

Another definition for useful heat is the absorber's capacity to transfer heat to the air, thereby increasing its enthalpy (temperature). This measure signifies the thermal performance of the receiver, leading to the determination of the convective heat transfer coefficient, which can be quantified as shown in Eq. (10).

$$Q_u = m \times c_p \times (T_{mo} - T_{mi}) = h_{ave} \times A_{pi} \times (T_{pm} - T_{fm}) \tag{10}$$

where T_{mo} and T_{mi} are the outlet and inlet bulk temperature of the air, while T_{pm} and T_{fm} are the average absorber and fluid temperature inside the absorber, while A_{pi} is the internal heat transfer area between the solid and fluid and h_{ave} represents the average internal heat convection coefficient. As the temperature is not uniform across the fluid inlet and

outlet cross-sectional areas, the mean inlet and out temperatures are determined using Eq.1, while the bulk fluid mean temperature difference can be expressed as Eq. (11).

$$T_{fm} = \frac{T_{mo} + T_{mi}}{2} \tag{11}$$

The h_{ave} derived from Eq. (10) is subsequently employed to ascertain the average Nusselt (Nu) number. The Nu number serves as a widely recognized indicator of heat transfer coefficients and is defined in Eq. (12).

$$Nu = \frac{h_{ave} \times D_{pi}}{k} \tag{12}$$

In the next step, the dimensionless Reynolds number (Re) was determined as Eq. (13).

$$Re = \frac{\rho v D_{pi}}{\mu} \tag{13}$$

In which D_{pi}, v, ρ, μ and k are representing the absorber hydraulic diameter (assumed to be equal to the SP inner diameter), fluid inlet velocity, density, dynamic viscosity, and thermal conductivity. These properties are evaluated at the average fluid temperature between inlet and outlet, as indicated in Eq.11.

The Performance Evaluation Criterion (PEC) is determined as given in Eq. (14), which serves as an indicator of the heat transfer enhancement over the pressure drop of the new system in comparison to the standard case.

$$PEC = \frac{Nu/Nu_{SP}}{(f/f_{SP})^{1/3}} \tag{14}$$

where SP denotes the clear (non-porous) absorber, and f states the friction factor defined as Eq. (15).

$$f = \frac{2}{L/D_i} \frac{\Delta p}{\rho v^2} \tag{15}$$

3. Validation results

In this section, the validation of the numerical models for the three samples (SP, 20RR, and 40RR) is presented sequentially. Initially, the accuracy of the RR porous geometries is verified in terms of pressure drop over the samples. Subsequently, the thermal model is applied to the SP sample and results are compared against the experimental data to assess the overall model accuracy. Next, the RR geometries (verified by pressure drop comparison) and thermal model (verified by the SP sample) are applied to the 20RR sample with the extremist working conditions (20030) to investigate the impact of the RR thermal conductivities, RR randomness, and turbulence models on the thermal behavior of the tube. Then, the derived conclusions from the sensitivity study are used under a wide range of working conditions to verify the
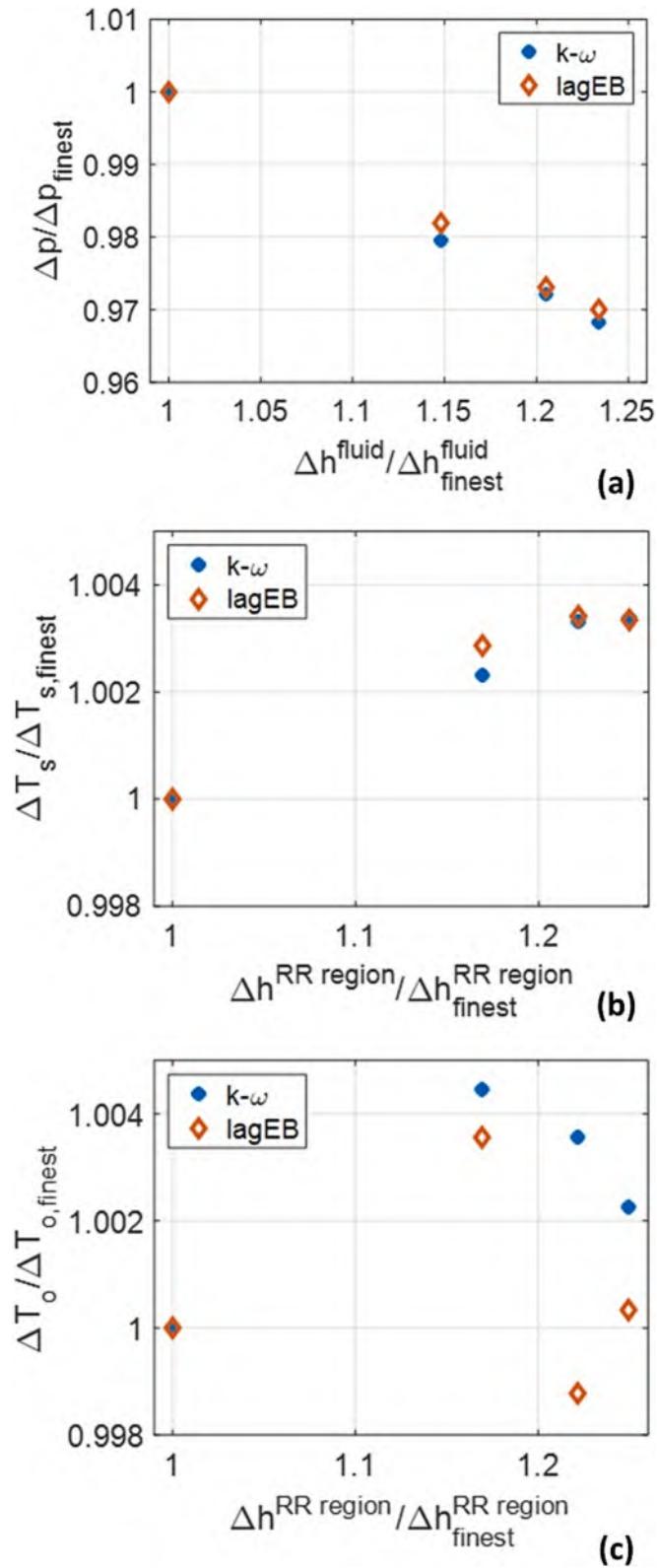
Fig. 8. Results with the different grids for the 20RR sample: (a) pressure drop, (b) maximum solid temperature and (c) outlet temperature.

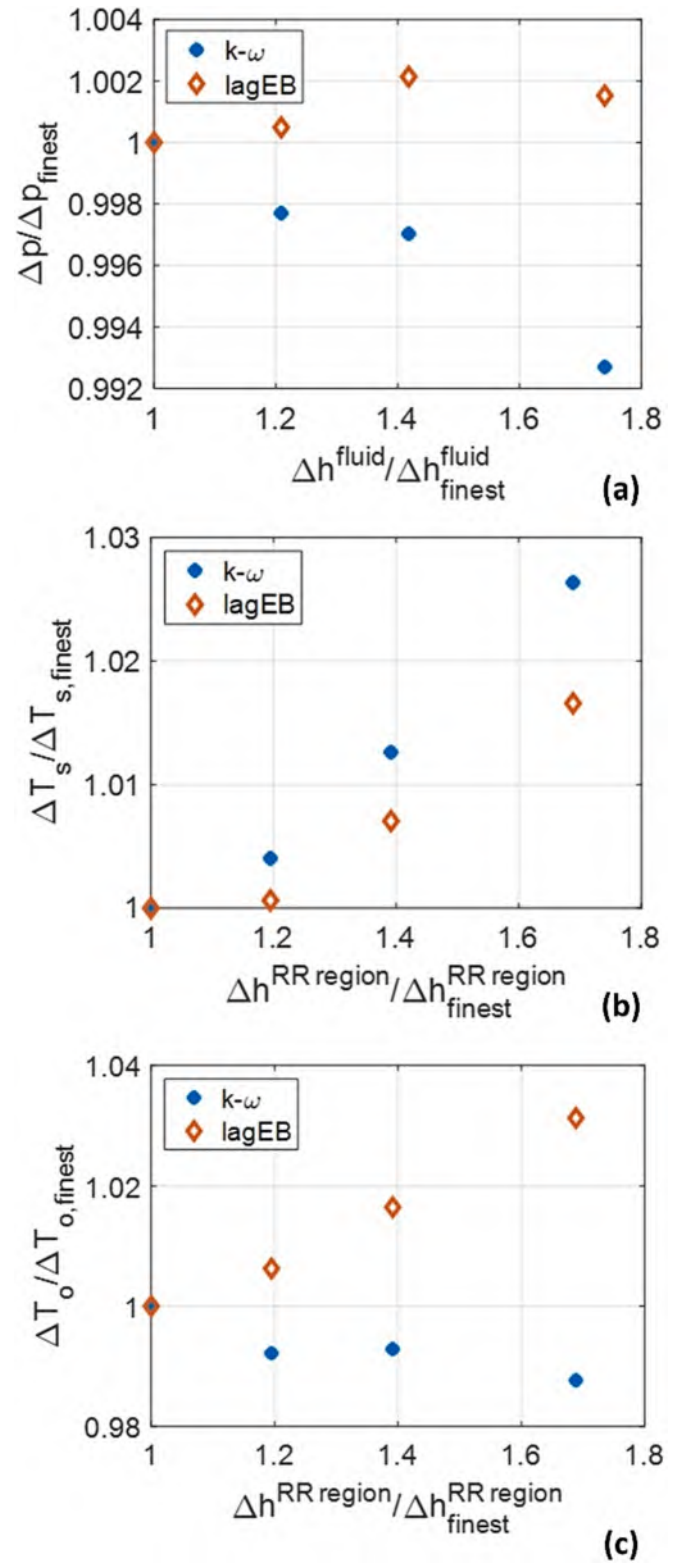**Fig. 9.** Results with the different grids for the SP sample: (a) pressure drop, (b) maximum solid temperature and (c) outlet temperature.

generality of the results against the experiments. Finally, the approved model with the selected parameters is implemented to the 40RR sample and compared against the experiments to verify the generality of the RR thermal model developed in the modeling phase.

3.1. Validation of pressure drop

Fig. 10 presents a comparison between the CFD and experimental data obtained for the 20RR and 40RR models. It is important to note that the simulations are performed in the absence of heat load and assumed isothermal sample operation, consistent with what was observed during
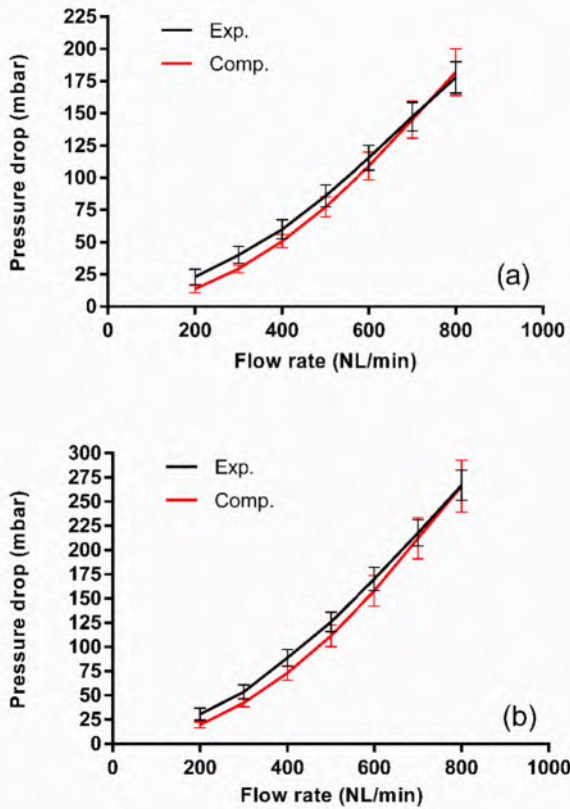
Fig. 10. Validation of the experimental pressure drop data against the numerical models; (a) 20RR sample, (b) 40RR sample.

Fig. 11. SP sample in the 20030 test condition: comparison of the tube wall temperature increase obtained with the experiments and CFD simulations, using two different turbulence models.

Fig. 12. SP sample: validation of the numerical study against the experimental test data in terms of hotspot temperatures. The computed values were obtained using the $k-\omega\,SST$ turbulence model.

the hydraulic experiments. In the tested flow rate range, it is evident that a very good agreement with less than a 2 % average error is achieved for the two models. Also, increasing the airflow rate improves the accuracy of the numerical models where the minimum deviation is recorded for the flow rate of 800 NL/min. This verifies the accuracy of the RR geometries developed for the two tested RR samples, providing consistent porosity and permeability compared to the experiments.

3.2. Validation of thermal model on SP

3.2.1. Effects of the turbulence models

Fig. 11 provides a detailed comparison between the experimental data obtained by the three thermocouples mounted on the backside of the SP sample with those extracted from the CFD simulations using the two different turbulence models. In general, the overlaps between the experimental and numerical error bars obtained by the two models indicate the consistency of the developed thermal models for simulating the experiments in the SP sample. Comparing the total average errors computed through the three temperature readings, the $k-\omega\,SST$ model demonstrates better accuracy in predicting the tube wall temperature rise, with an accuracy 1 % higher than the lagEB $k-\varepsilon$ model. As a result, the $k-\omega\,SST$ model was employed for simulating other test conditions to assess the repeatability of the developed model in SP sample.

3.2.2. Validation on all the test modes

In Fig. 12, the thermal model has been applied to all test conditions of the SP sample, and it represents the comparison between the numerical and experimental data obtained from thermography on the front side of the sample (Hotspot temperature). As depicted, a very good agreement is consistently observed across all test conditions. This
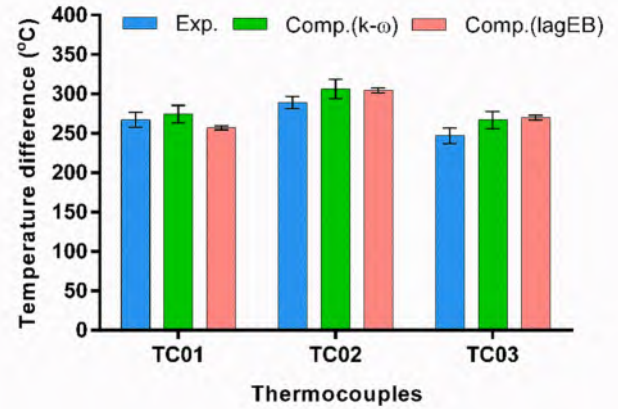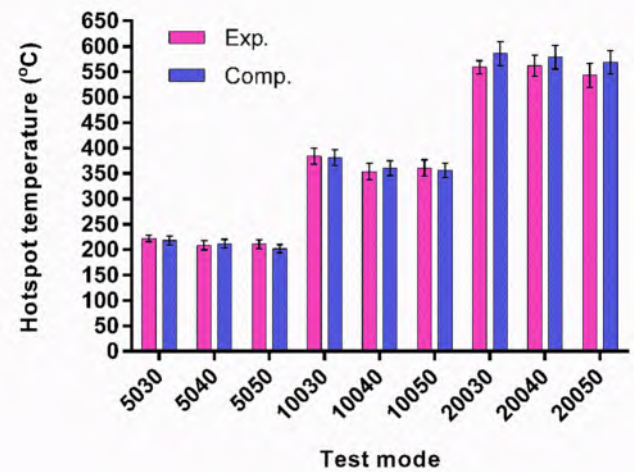
substantiates the validity of the thermal model, including the applied heat and heat losses developed in this study.

3.3. Validation of thermal model on 20RR

3.3.1. Effects of the turbulence models

Temperature comparisons for the seven thermocouples on the 20RR sample are presented in Fig. 13, highlighting the effects of the turbulence models on the tube wall temperature measurements. As also observed in Fig. 11, the $k-\omega\,SST$ model consistently provides more accurate thermal results compared to the lagEB $k-\varepsilon$ model. However, it is worth noting that in two specific spots displayed by TC03 and TC04, the lagEB performs better than the $k-\omega\,SST$ model, especially in the case of TC04. TC04 is located above the RR region and is strongly influenced by the flow inside the RR pore zones. For the regions located both upstream and downstream of the porous medium, the SST model outperforms lagEB model. This possibly may be due to the zero and lower mixing and splitting of fluid streams in those regions. The overlaps between the experimental and numerical errors further substantiate the applicability of the thermal model developed for the SP sample to the RR samples, thus validating the simulations.
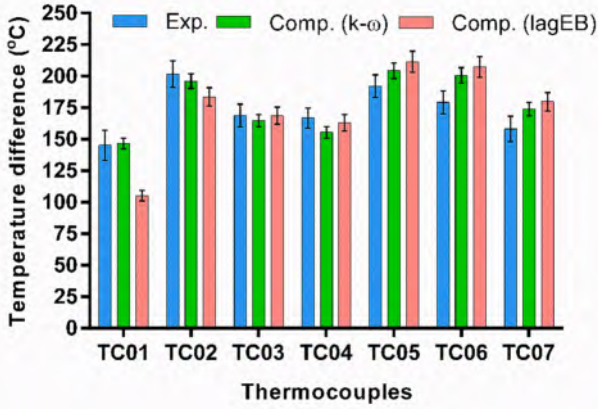
Fig. 13. 20RR sample in the 20030 test condition: comparison of the tube wall temperature increase obtained with the experiments and CFD simulations, using two different turbulence models.

3.3.2. Effects of the RR randomness

To account for the randomness of the contacts between the RRs and tube inner wall and explore their effects on the temperature measurements, the heat load was azimuthally rotated around the 20RR sample in the selected simulation (20030 test mode). The results were compared among 4 different configurations and are illustrated in Fig. 14. As expected, TC01 and TC02, which are located upstream of the heated region, exhibit no significant effects depending on the heat load location. While some effects are noticeable for the thermocouples located under the heated zone, or downstream, the maximum standard deviation among the four CFD models is nearly 1.5 °C (observed at TC04). The overlaps between the computed and experimental data demonstrate the validity of the numerical models, irrespective of the heat load orientation. This indicates that the effects of RR randomness on temperature measurements are not significant and can be safely disregarded.

3.3.3. Effects of the RR thermal conductivity

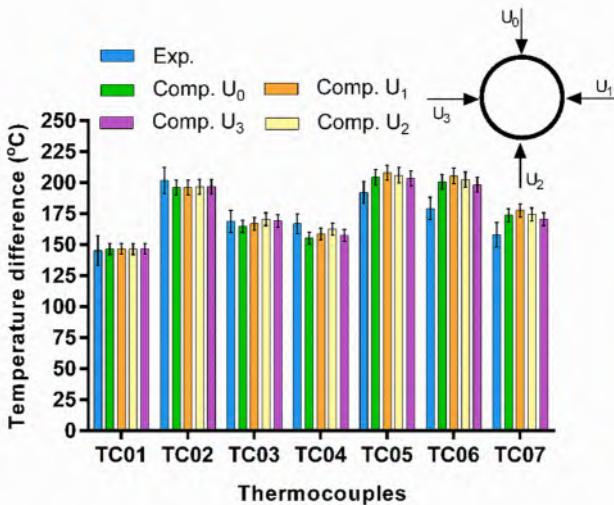To investigate the dependency of the thermal results on the ETC of the porous medium, various thermal conductivity values of the RR matrix were considered in the 20RR sample working under 200 kW/m^2 solar peak load and 30 NL/min airflow rate, and results are reported in Fig. 15. As it can be observed, a negligible effect is computed for all the temperature measurements. This lack of impact can be attributed to the spot contacts between the RRs (and between the RR and the tube), which indicate limited thermal conduction between the particles. As a consequence, the numerical results appear to be independent of the ETC, and a value of 500 W/mK was selected and used for further simulations.

3.3.4. Validation on all the test modes

The thermal model was applied also to the wide range of test conditions and results are reported in Fig. 16, to be compared against the experimental data in terms of hotspot temperature from the front side of the samples. As depicted, there is a high degree of agreement between the numerical and experimental results, confirming the validity of the thermal model in simulating RR samples.

3.4. Validation of thermal model on 40RR

3.4.1. Validation on the wall temperature profile

The selected turbulence model ($k - \omega\, SST$ mode) is used to predict the tube wall temperature increase on the 40RR sample, and results are reported in Fig. 17, considering a solar peak load of 200 kW/m^2 and 30 NL/min airflow rate. As already discussed, the $k - \omega\, SST$ model has demonstrated its ability to provide accurate results based on the experimental data with an average error of $\sim$ 4 % between the mean values. Moreover, the overlaps between the experimental and CFD results validate the consistency of the developed thermal model for the entire length of the 40RR sample.

3.4.2. Validation on all the test modes

The results of the numerical simulation developed for the 40RR sample in terms of hotspot temperature are provided in Fig. 18 for all the different test modes. The developed CFD model exhibits good accuracy in reproducing all the experimental conditions and results, with an average error of $\sim$ 5 % between the mean values of the temperatures. As a result, the overall agreement is satisfactory and underscores the suitability of the numerical simulations applied to RR models for further analyses.
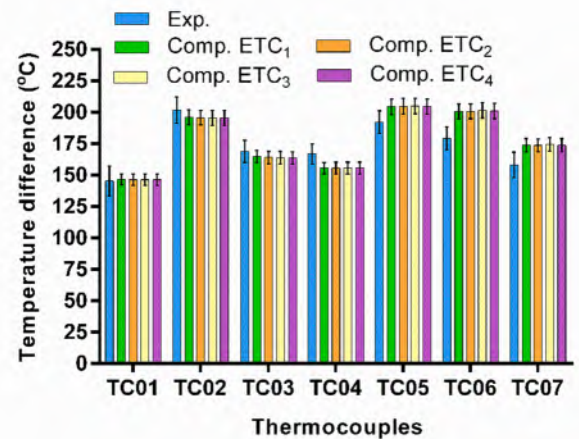

Fig. 14. 20RR sample in the 20030 test condition: comparison of the tube wall temperature increase obtained with the experiments and CFD simulations, using different heat load orientations. The computed values were obtained using the $k - \omega\, SST$ turbulence model.

Fig. 15. 20RR sample in the 20030 test condition: comparison of the tube wall temperature increase obtained with the experiments and CFD simulations, using different RR thermal conductivities [ETC$_1$ = 500 W/mK, ETC$_2$ = 1500 W/mK, ETC$_3$ = 2500 W/mK, and ETC$_4$ = 3500 W/mK]. The computed values were obtained using the $k - \omega\, SST$ turbulence model.
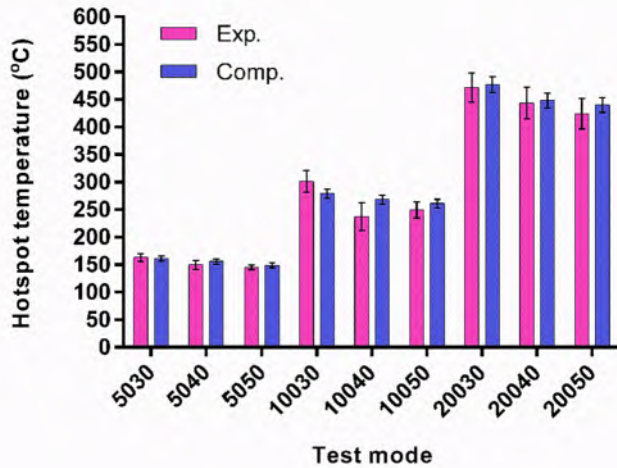
Fig. 16. 20RR sample: validation of the numerical study against the experimental test data in terms of hotspot temperatures. The computed values were obtained using the $k-\omega\,SST$ turbulence model.
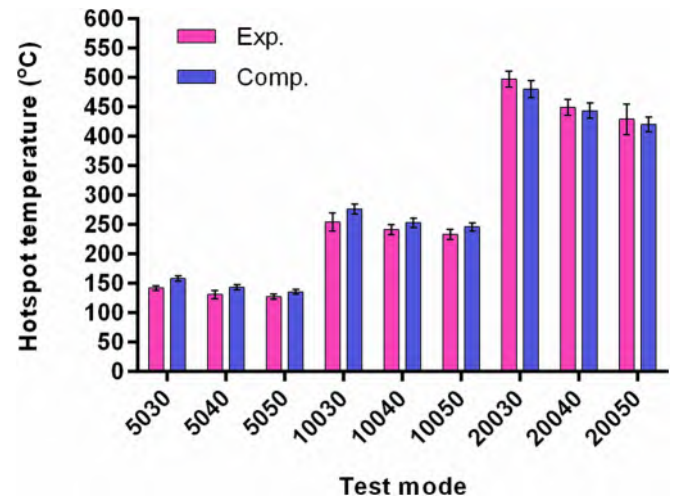

Fig. 18. 40RR sample: validation of the numerical study against the experimental test data in terms of hotspot temperatures. The computed values were obtained using the $k-\omega\,SST$ turbulence model.
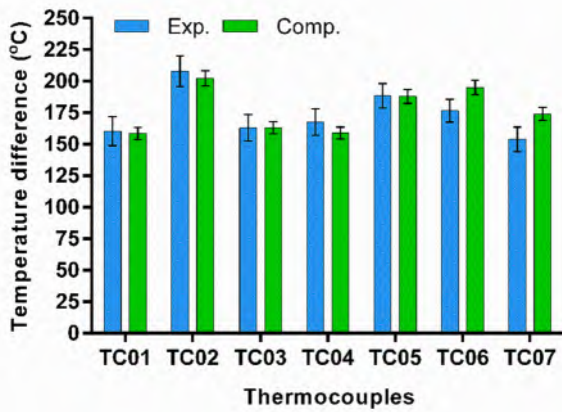

Fig. 17. Comparison of the tube wall temperature increase obtained with the experiments and CFD simulations, using the $k-\omega\,SST$ turbulence model for the 40RR sample at 20030 test condition.

4. Detailed thermo-hydraulic analysis

This section provides a detailed analysis of the hydraulic and thermal behavior of air passing through the porous medium and employs some key parameter indicators such as *f* and *Nu* to investigate the optimum performance.

4.1. Hydraulic performance

Fig. 19 illustrates the velocity map on the different cross sections for the 40RR sample working with 30 NL/min airflow rate and 200 kW/m^2 solar peak flux. As shown, the random packing configuration of the RR porous structure has resulted in high-velocity flows in axial and azimuthal directions, resulting in irregular pattern inside the porous zone. One of the observed hydraulic peculiarities is the flow channeling occurring in the void spaces between the rings, which is more highlighted in the second half of the porous medium due to the increased speed of the air proceeding through the porous zone. According to the three azimuthal cross sections, section A-A represents the flow regime at the porous insert upstream, in which the airflow is smooth and fully developed, where the boundary layers are formed and thick. Section B-B
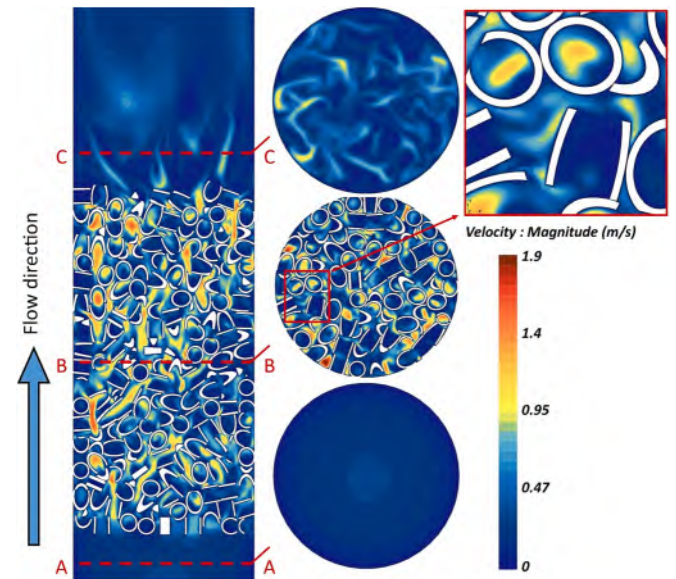

Fig. 19. Velocity field with cross sectional views for fluid flow through the 40RR sample using 30 NL/min and 200 kW/m^2.

shows a cross section in the middle of the porous medium and clarifies that ring orientations are very effective in forming the velocity streams in the packed structures. In other words, when an air stream reaches a ring rested axially with respect to the flow direction, it is forced to pass through the narrow ring inner space, creating an accelerated fluid motion that improves the flow turbulence (see zoom section). On the other hand, when the air faces a RR ring perpendicular to the flow direction, it passes the RR without an inner flow and air stagnation occurs inside the ring. Section C-C, which is formed by a cross section at the porous insert downstream, reflects the chaotic flow at the exit of the RR insert where a number of vortices are generated due to the uneven flow discharge promoted by the random RR orientations. This behavior enables high-velocity flow streams near the tube wall, creating narrow thermal boundary layers and enhancing the heat transfer at the tube downstream.

Pressure drop maps of the two samples working with 30 NL/min airflow rate and 200 kW/m^2 solar peak flux are depicted in Fig. 20, with a zoom-section view of the porous zone. For the two domains, the
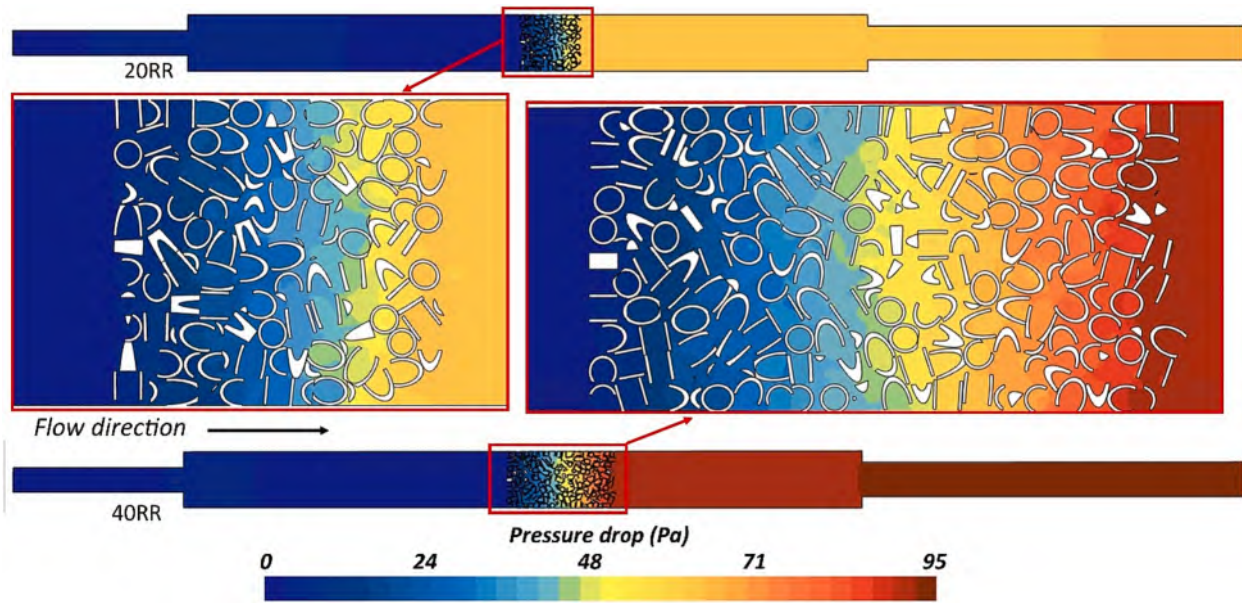
Fig. 20. Pressure drop distribution along the flow direction on a longitudinal cross section for fluid flow through the 20RR and 40RR sample using 30 NL/min and 200 kW/m².

highest pressure loss occurs within the RR region, where it accounts for 93.5 and 90 % of the total pressure drop measured over 40RR and 20RR samples, respectively. Moreover, growing the RR layers has a nonlinear impact on the increase in ΔP, in which changing the porous length from 20 to 40 mm intensifies the ΔP over the insert by 57 %.

The air pressure uniformity with the surface average on different azimuthal cross sections for the porous length ratio is depicted in Fig. 21. According to the similar trends found for the two samples, pressure uniformity starts from near 0.5 at the early points and increases up to 0.98, reaching the middle length (l/L ~ 0.5). Then moving through the second half, air pressure uniformity decreases, returning to the initial value of ~ 0.5. This flow behavior is attributed to the fact that air pressure is highly affected by the boundary conditions at the inlet and outlet porous faces. Furthermore, the generation of recirculation flows at both regions (porous inlet and outlet) leads to high adverse pressure gradients and less pressure uniformity due to the flow obstructions by RRs. A similar pattern was also reported by Wu et al. [59] where different flow states were observed in the upper, middle, and lower parts of the main channel for a gas flowing through the particle bed.

To assess the amount of pressure that is sacrificed because of the porous inserts, Fig. 22 shows the ratio of friction factors computed
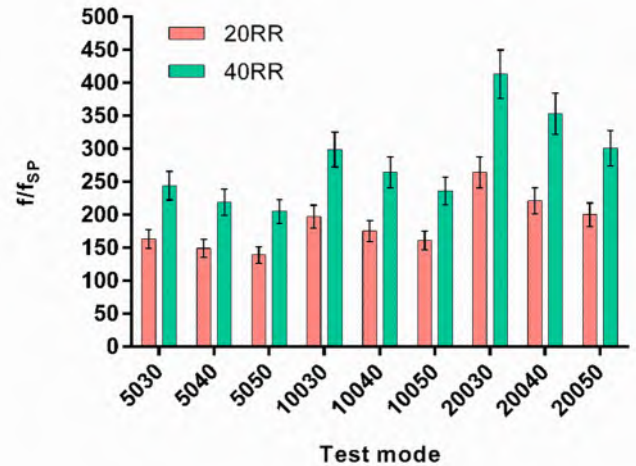

Fig. 22. The comparison of growth in the friction factors produced by the RR inserts corresponding to the SP absorber (f/f$_{SP}$) for various test conditions.

between the modified and smooth tubes. In order to make a fair comparison with only the effects of the inserts, the pressure drops are obtained upon the two cross sections made at the inlet and outlet of the tube sample area (see Fig. 5a), excluding the entrance and exit sections. It is observed that at the constant solar peak flux, increasing the mass flow rate has decreased the growth in the pressure drop with respect to the smooth pipes. Moreover, at the same airflow rate, increasing the solar peak flux enlarges the growth in friction factor ratio, and this roots in more significant drops in the air density at higher temperatures and consequently higher flow velocity inside the porous region. Therefore, the highest ratios for the two samples were recorded as 400 and 250, respectively for 40RR and 20RR, working at an airflow rate of 30 NL/min and a solar flux of 200 kW/m².

Fig. 23 provides the ratio of values of the pressure drop over the porous length computed for the two models with respect to a variety of superficial air velocities obtained by isothermal simulations. Based on the Darcy–Dupuit–Forchheimer model, well-explained in the experimental work [49], the values of the viscous (β) and inertial resistance (C) coefficients in
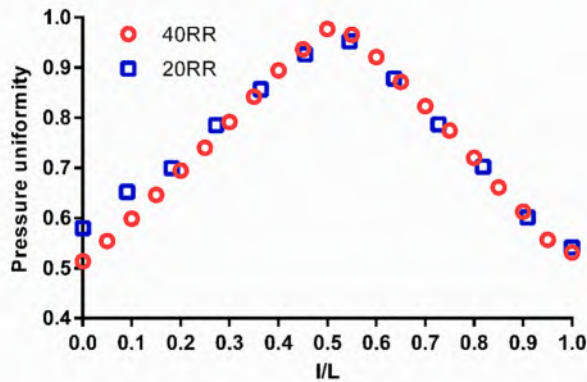

Fig. 21. Pressure uniformity based on azimuthal averaging along the flow direction through the 20RR and 40RR sample using 30 NL/min and 200 kW/m².
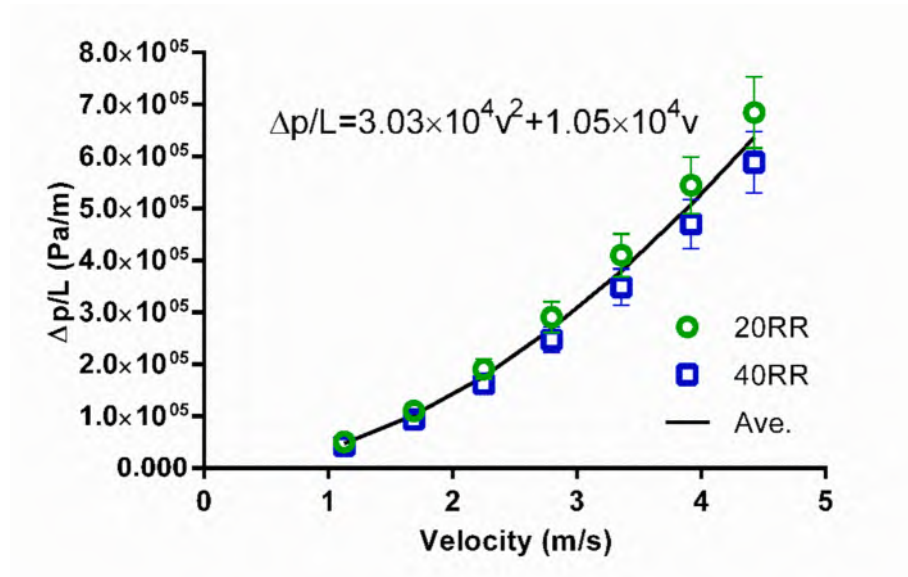
Fig. 23. The relationship between the pressure drop and superficial air velocity ($\Delta P/L$) computed over the porous medium. [L is the porous length and ΔP is the pressure difference over the porous insert].

the direction of the airflow can be extracted from the parabolic curve. The comparison of the CFD coefficients of $1/\alpha$ and C as 5.68×10^8 m^{-2} and 5.77×10^3 m^{-1} with those of the experiments as $7.13 \times 10^8 \pm 4.85 \times 10^8$ m^{-2} and $5.37 \times 10^3 \pm 5.6 \times 10^2$ m^{-1} proves the similarities of the hydraulic characteristics obtained from the real RR structures and simulations.
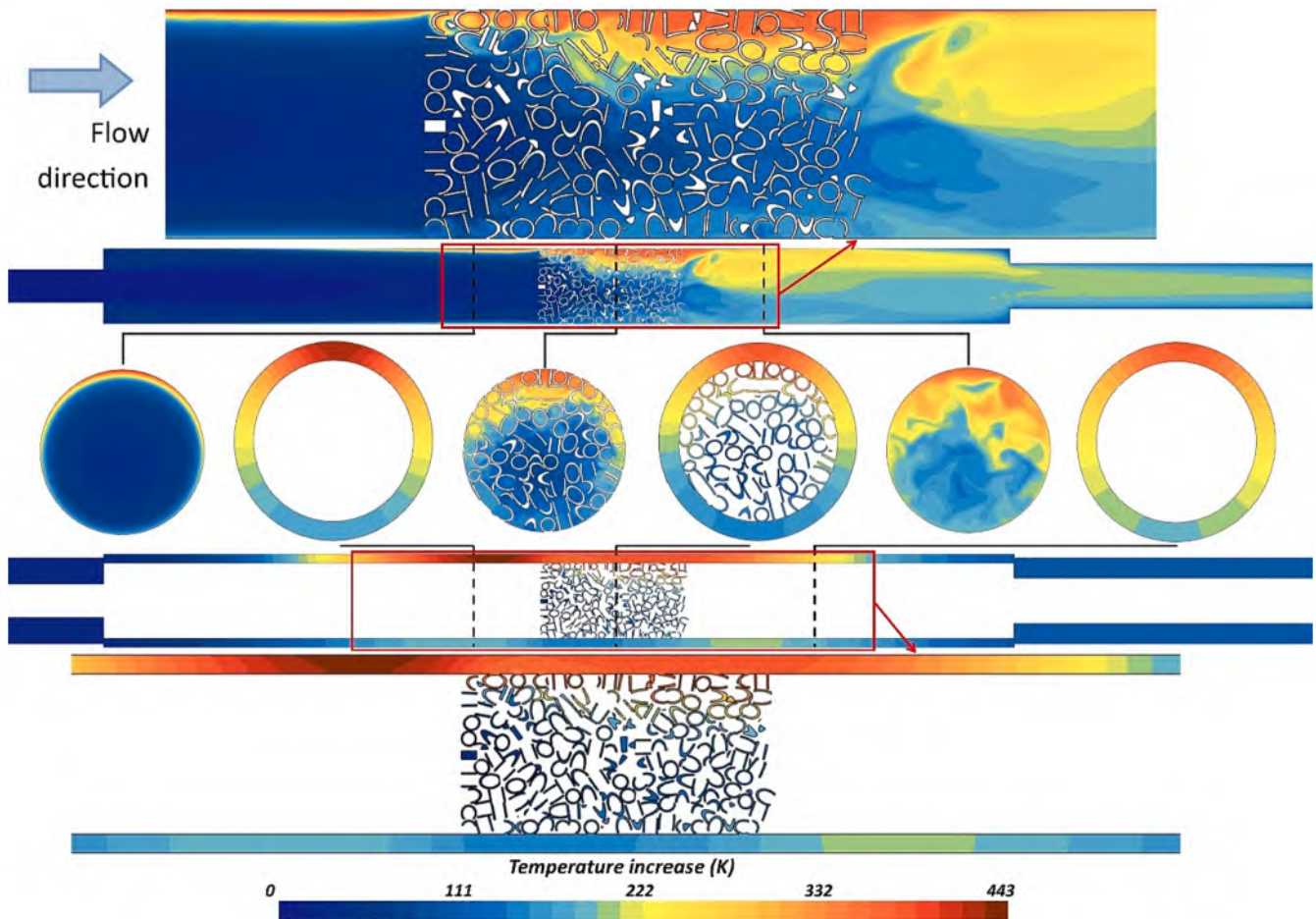

Fig. 24. Fluid and solid temperature increase with respect to the fluid inlet temperature along the flow direction on a longitudinal cross section for fluid flow through the 40RR sample using 30 NL/min and 200 kW/m^2.

4.2. Thermal performance

Temperature distribution of the fluid and solid domains on different longitudinal and azimuthal cross sections are depicted in Fig. 24, considering the 40RR model using 30 NL/min and 200 kW/m². According to the longitudinal fluid section, the extended heat transfer area along with the air thermal mixing in the porous medium has promoted a high heat transfer within the RR region. Furthermore, the solid temperature map highlights the cooling effects of the RR insert on the wall temperature. Hence, the hotspot shifts toward the upstream, where the thick air thermal boundary layers with low-temperature gradients act as insulation and hinder an effective thermal exchange. However, the tube wall temperature at the tube downstream remains cooler due to the high turbulence fluid regime and an improved heat transfer rate. It is worth noting that the appearance of a local hotspot on the insert downstream and tube backside refers to the flow recirculation and the stationary vortex formed as the result of the packed structure, which resists the heat transfer in that particular location. Thus, the local temperature on the absorber wall increases in that zone. Three azimuthal cross sections are also extracted on the fluid and solid domains in which the upstream sections demonstrate the low heat transfer rate from the tube wall to the fluid core zone. However, the azimuthal cross sections on the RR region, imply the role of three RR layers in heat penetration through the fluid stream and show how thermal mixing is enhancing the heat removal from the tube wall. The temperature maps on the downstream cross sections reflect the swirl flow at the porous discharge and how thermal mixing continues to decrease the tube wall temperature at that region.

The profiles of tube wall temperature rise with respect to the fluid inlet temperature are computed on the front side of the three samples, under the same conditions (30 NL/min and 200 kW/m²) and depicted in Fig. 25. As shown, for all samples, the tube temperature rise follows a gaussian pattern similar to the solar heat flux, where the trend starts from an initial value, then reaches to the peak in the middle of the tube (distance = 117.5 mm), and diminishes to a final value, which is higher than the initial. The trend of the SP model shows a larger temperature difference all over the tube compared to the two modified tubes, which shows that RR inserts in addition to the RR regions are also able to cool the entire absorber. Moreover, the insertion of RR porous media changes the temperature rise profiles from a one-peak to a two-peak where the second peak is reduced due to the enhanced air thermal performance at porous downstream. The prolonged porous integration in the 40RR model provides a longer cooled distance and this has affected significantly the second temperature peak. Comparing the tube wall temperature rise in the location of the peak solar flux shows that the porous inserts are reducing it by 30 and 32 % for 20RR and 40RR samples,
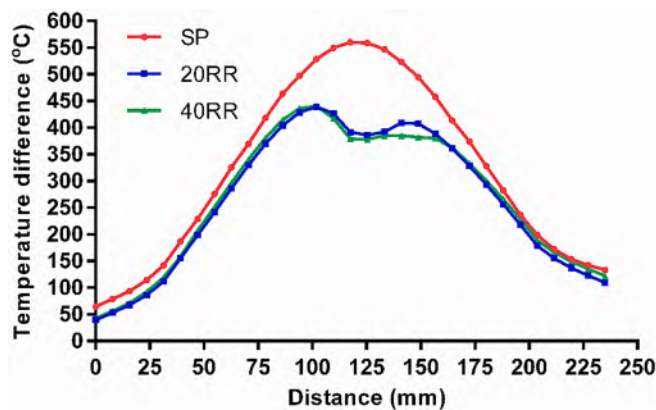
respectively. Thus, the peak thermal losses are decreased, and the total thermal performance of the solar absorber increases.

Fig. 26 provides the ratio between the Nu number computed for the modified tube and those of the smooth pipe, depending on the test mode. As shown, increasing the solar heat flux improves the Nu augmentation ratio, where 200 kW/m² exhibits the highest ratio for the two models. The reason for this behavior can be attributed to the deeper heat distribution within the RR particles at higher solar flux and consequently larger heat flow from the solid to the fluid medium compared to the clear tube. On the other side, at a given solar peak flux, the growth in airflow rate, decreases the enhancements in Nu number compared to the standard case, which shows that the rise in the airflow turbulence diminishes the positive effects of RR medium in heat transfer augmentation. Moreover, the 40RR tube represents a higher ratio than 20RR which is due to the larger heat transfer area and more heat exchange. As a result, the maximum ratio was achieved as 16 for the 40RR tube which operates with 30 NL/min airflow rate and 200 kW/m² solar peak flux, which is nearly 45 % growth compared to that of the 20RR model.

To elaborate on the total thermo-hydraulic performance of the absorber tubes and find the best working condition, the computed values of PEC are given in Fig. 27. It can be seen that the 40RR sample has higher values of PEC than the 20RR samples which proves that the rise in the Nu number due to the higher heat transfer area overcomes the larger pressure drops for this tube and puts it as a better option, as far as the performance augmentation with RR porous media is concerned. The values obtained for the 20RR tube range from 1.5 to 1.9, and for the 40RR from 2 to 2.4, which justifies that in all the test cases the usage of RR inserts is more efficient than the smooth tube. The 30 NL/min airflow rate shows the best operating condition at all the heat flux levels, due to an offset between the increase in Nu and pressure drop, where the maximum PEC number is obtained at the solar peak flux of 50 kW/m², using 40RR sample. This concludes that the integration of RR porous inserts under lower airflow rates and reduced solar radiations is more impactful. The PEC values obtained are consistent with the range reported by Savoldi et al. [48] (2–2.5) for the same porous material used at similar airflow rates for CSP applications. Also, comparing the highest PEC value computed in this study with those reported in the literature shows the superiority of RR porous inserts for tubular solar receivers with 41 % than the porous design proposed by Das et al. [60], 50 % than the metal foam inserts reported by Wang et al. [61], 30 % than the configurations used by Zheng et al. [62], more than 100 % with copper foams proposed by Jamal-Abad et al. [32], and 10 % than the porous foams employed by Soo Too and Benito [63]. Moreover, it should be

Fig. 25. Wall temperature increase distribution with respect to the fluid inlet temperature on the front side of the SP, 20RR, and 40RR absorbers along the flow direction, using 30 NL/min and 200 kW/m².
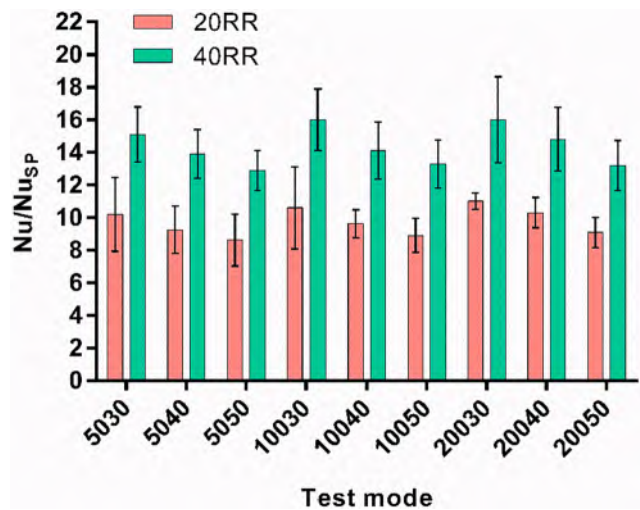

Fig. 26. The comparison of growth in the Nusselt number produced by the RR inserts corresponding to the clear absorber (Nu/Nu$_{SP}$) for various test conditions.
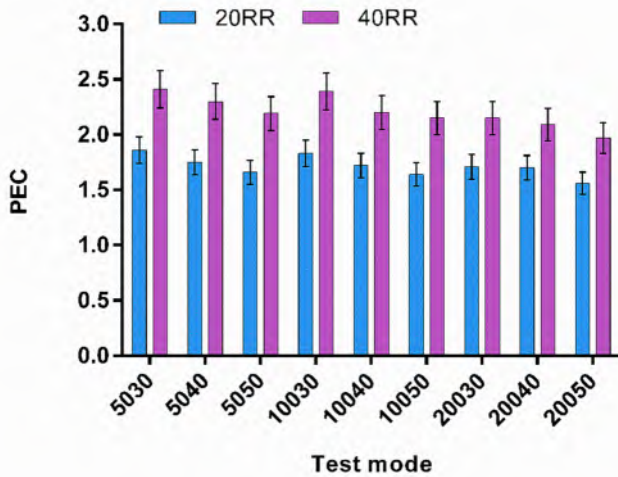
Fig. 27. The comparison of computed PEC produced by the RR inserts for various test conditions.

noted that the integration length of the RR porous media in this study was only 12.5 % and 25 % of the heated area respectively for 20RR and 40RR samples compared to the 100 % coverage in all the previous cases. This implies that if RR porous inserts are integrated in small percentages, they still provide significant thermal enhancements compared to the other materials, especially for non-uniform heating applications, which could justify its higher cost over other designs.

5. Conclusions

In this study, a numerical model was developed at the pore-scale to explore the thermo-hydraulic behavior of a porous insert made of metallic RRs and integrated with gaseous tubular solar absorbers. A set of experiments were utilized to validate the accuracy of the CFD results and investigate the effects of some modelling parameters such as turbulence model, porous effective thermal conductivity, and porous particle randomness on the developed model. The validation results confirmed the applicability of the proposed model and indicated the reliability of the generated packed bed as the porous medium through the DEM method. As long as the porous material comprises packed bed elements, the instructions and methodology discussed in this paper are applicable. As demonstrated in this study, DEM simulations can provide the geometry of advanced packed porous materials. The details provided in the sensitivity results of different numerical parameters can be further utilized for simulating other porous geometries with similar features.

Comparisons between the basic (SP) and enhanced (20RR and 40RR) samples revealed the positive impact of RR integration on performance augmentation across a wide range of working conditions. From this analysis, the major conclusions are listed as follows.

1. The analysis shows that the $k-\varepsilon$ lagEB model has slightly lower accuracy in predicting fluid temperature at porous medium upstream and downstream, especially around the entrance section. This may attribute to the fact that there is no flow mixing and splitting at that section. However, the $k-\omega SST$ model was selected due to the precisions in estimating fluid temperature distribution all over the domain.
2. A comparison of the simulated tube wall temperature by the four different flux orientations to express the effects of the RR randomness and random contacts to the tube shows that a negligible difference of nearly 1.5 °C could appear between the CFD temperature measurements.

3. Changing the porous ETC values in the same model, the thermal results are found to be independent of the thermal conductivity, which refers to the spot contacts between the porous particles. Thus, the value of 500 W/mK, which was the closest to the base material (copper) was selected and used in the simulations.
4. Flow study indicates the velocity irregularity in air passage through the RR zone, where some flow channelings were observed in the void space between the rings as well as stagnation points. Moreover, the arbitrary structure of the porous medium leads to an uneven flow discharge at the porous outlet, driving a chaotic flow, which includes some small vortices at the porous insert downstream.
5. Increasing the solar peak flux at the same airflow rate decreases the fluid density and rises the fluid velocity in the porous medium. This leads to a ~ 20 growth in the computed pressure drops for 20RR and 40RR samples, working at 50 NL/min airflow rate and rising the solar peak flux from 50 to 200 kW/m^2. Thus, the maximum pressure drops were found at the 20050 tests, as ~ 14 Pa, ~122 Pa, and ~ 190 Pa for SP, 20RR, and 40RR samples, respectively.
6. The uniformity of the air pressure drop through the azimuthal averaging indicates that the maximum index (~0.98) is observed in the middle of the porous medium, while the generation of recirculation flows at the porous inlet and outlet faces provides high adverse pressure gradients and less pressure uniformity (~0.5).
7. The analysis of the f/f$_{SP}$ reveals that the rise in the airflow rate has diminished the growth in the friction factor, indicating that the increased pressure drop in the smooth tube overcomes the negative effects of porous inserts on the total pressure drop.
8. Using the RR porous inserts, the tube wall hotspot point shifts toward the insert upstream while the downstream is affected by an increased turbulence fluid regime and an improved heat transfer rate. Analysing the tube wall temperatures in the location of the peak solar flux, a 30 and 32 % reduction are seen for 20RR and 40RR samples working under 30 NL/min airflow rate and 200 kW/m^2 solar peak flux.
9. Comparison of the Nu/Nu$_{SP}$ between the enhanced pipes displays the positive role of solar peak flux on the Nu ratio enhancement, where the maximum is > 15 and > 10 for the 40RR and 20RR samples working under 30 NL/min airflow rate and 200 kW/m^2 solar peak flux.
10. Finally, the performance of the RR samples was evaluated in terms of PEC, in which 40RR outweighs the 20RR sample, showing that the rise in Nu number overcomes the increased friction factors. Moreover, the comparison between the proposed porous insert with the reported models in the literature demonstrates the potential advantage of the RR in enhancing the overall efficiency of tubular solar absorbers.

From the perspective of this work, it is crucial to conduct an optimization study on the length of the porous material, with a focus on understanding the interplay between the applied heat and the length of the RR inserts. This investigation will contribute to the development of the ultimate design for a solar receiver used as billboards. The design will incorporate multiple tubes enhanced with RR porous inserts of varying lengths, accounting for the distribution of heat load.

Declaration of competing interest

The authors declare that they have no known competing financial interests or personal relationships that could have appeared to influence the work reported in this paper.

References

[1] S. Rashidi, J.A. Esfahani, F. Hormozi, Classifications of porous materials for energy applications, Encycl. Smart Mater. (2021) 774–785, https://doi.org/10.1016/B978-0-12-803581-8.11739-4.

[2] S. Rashidi, J.A. Esfahani, A. Rashidi, A review on the applications of porous materials in solar energy systems, Renew. Sustain. Energy Rev. 73 (2017) 1198–1210, https://doi.org/10.1016/j.rser.2017.02.028.

[3] S.J. Shbailat, M.A. Nima, Possible energy saving of evaporative passive cooling using a solar chimney of metal foam porous absorber, Energy Convers. Manag. x. 12 (2021), 100118, https://doi.org/10.1016/j.ecmx.2021.100118.

[4] S. Aghakhani, M. Afrand, Experimental study of the effect of simultaneous application of the air- and water-cooled flow on efficiency in a Photovoltaic thermal solar collector with porous plates, Appl. Therm. Eng. 217 (2022), 119161, https://doi.org/10.1016/j.applthermaleng.2022.119161.

[5] H. Wang, Q. Wu, Y. Mei, L. Zhang, S. Pang, A study on exergetic performance of using porous media in the salt gradient solar pond, Appl. Therm. Eng. 136 (2018) 301–308, https://doi.org/10.1016/j.applthermaleng.2018.03.025.

[6] S. Shoeibi, M. Saemian, H. Kargarsharifabad, S. Hosseinzade, N. Rahbar, M. Khiadani, M.M. Rashidi, A review on evaporation improvement of solar still desalination using porous material, Int. Commun. Heat Mass Transf. 138 (2022), 106387, https://doi.org/10.1016/j.icheatmasstransfer.2022.106387.

[7] N. Prasanth, M. Sharma, R.N. Yadav, P. Jain, Designing of latent heat thermal energy storage systems using metal porous structures for storing solar energy, J. Energy Storage. 32 (2020), 101990, https://doi.org/10.1016/j.est.2020.101990.

[8] H. Zhang, Y. Shuai, B.G. Lougou, B. Jiang, F. Wang, Z. Cheng, H. Tan, Effects of multilayer porous ceramics on thermochemical energy conversion and storage efficiency in solar dry reforming of methane reactor, Appl. Energy. 265 (2020), 114799, https://doi.org/10.1016/j.apenergy.2020.114799.

[9] S. Singh, Experimental and numerical investigations of a single and double pass porous serpentine wavy wiremesh packed bed solar air heater, Renew. Energy. 145 (2020) 1361–1387, https://doi.org/10.1016/j.renene.2019.06.137.

[10] S. Singh, Utilising fractional porous interface for high thermal performance of serpentine wavy channel solar air heater, Appl. Therm. Eng. 205 (2022), 118044, https://doi.org/10.1016/j.applthermaleng.2022.118044.

[11] R. Khatri, S. Goswami, M. Anas, S. Sharma, S. Agarwal, S. Aggarwal, Performance evaluation of an arched plate solar air heater with porous aluminum wire mesh cylindrical fins, Energy Reports. 6 (2020) 627–633, https://doi.org/10.1016/j.egyr.2020.11.177.

[12] Q. Xiong, T. Tayebi, M. Izadi, A.A. Siddiqui, T. Ambreen, L.K.B. Li, Numerical analysis of porous flat plate solar collector under thermal radiation and hybrid nanoparticles using two-phase model, Sustain. Energy Technol. Assess. 47 (2021), 101404, https://doi.org/10.1016/j.seta.2021.101404.

[13] K. Anirudh, S. Dhinakaran, Numerical analysis of the performance improvement of a flat-plate solar collector using conjugated porous blocks, Renew. Energy. 172 (2021) 382–391, https://doi.org/10.1016/j.renene.2021.02.145.

[14] N.F. Jouybari, T.S. Lundström, Performance improvement of a solar air heater by covering the absorber plate with a thin porous material, Energy. 190 (2020), https://doi.org/10.1016/j.energy.2019.116437.

[15] A.L. Hernández, J.E. Quiñonez, F.H. López, Transient numerical study of thermo-energetic performance of solar air heating collectors with metallic porous matrix, Sol. Energy. 178 (2019) 181–192, https://doi.org/10.1016/j.solener.2018.12.035.

[16] Y. Cao, S. Hamidvand, M. Bezaatpour, M. Ebadollahi, H. Ghaebi, Microporous foam, magnetic nanoparticles, and revolutionary tubes: Sophisticated combination of three solar energy materials in flat plate solar collectors, Sol. Energy Mater. Sol. Cells. 235 (2022), 111464, https://doi.org/10.1016/j.solmat.2021.111464.

[17] H.J. Jouybari, S. Saedodin, A. Zamzamian, M.E. Nimvari, S. Wongwises, Effects of porous material and nanoparticles on the thermal performance of a flat plate solar collector: An experimental study, Renew. Energy. 114 (2017) 1407–1418, https://doi.org/10.1016/j.renene.2017.07.008.

[18] M.M.M. Salih, O.R. Alomar, H.N.S. Yassien, Impacts of adding porous media on performance of double-pass solar air heater under natural and forced air circulation processes, Int. J. Mech. Sci. 210 (2021), 106738, https://doi.org/10.1016/j.ijmecsci.2021.106738.

[19] S. Abo-Elfadl, M.S. Yousef, M.F. El-Dosoky, H. Hassan, Energy, exergy, and economic analysis of tubular solar air heater with porous material: An experimental study, Appl. Therm. Eng. 196 (2021), 117294, https://doi.org/10.1016/j.applthermaleng.2021.117294.

[20] D. Xu, M. Lin, International Journal of Heat and Mass Transfer Design controllable TPMS structures for solar thermal applications : A pore-scale vs. volume-averaged modeling approach, Int. J. Heat Mass Transf. 201 (2023), https://doi.org/10.1016/j.ijheatmasstransfer.2022.123625.

[21] S.A. Gandjalikhan Nassab, Y. Sheikhnejad, M. Foruzan Nia, Novel design of natural solar air heat for higher thermal performance utilizing porous vortex generator, Therm. Sci. Eng. Prog. 33 (2022), 101385, https://doi.org/10.1016/j.tsep.2022.101385.

[22] K. Ravi Kumar, K.S. Reddy, Thermal analysis of solar parabolic trough with porous disc receiver, Appl. Energy. 86 (2009) 1804–1812, https://doi.org/10.1016/j.apenergy.2008.11.007.

[23] K.S. Reddy, K. Ravi Kumar, C.S. Ajay, Experimental investigation of porous disc enhanced receiver for solar parabolic trough collector, Renew Energy 77 (2015) 308–319, https://doi.org/10.1016/j.renene.2014.12.016.

[24] S. Ebrahim Ghasemi, A. Akbar Ranjbar, Numerical thermal study on effect of porous rings on performance of solar parabolic trough collector, Appl. Therm. Eng. 118 (2017) 807–816, https://doi.org/10.1016/j.applthermaleng.2017.03.021.

[25] Z. Zheng, Y. Xu, Y. He, Thermal analysis of a solar parabolic trough receiver tube with porous insert optimized by coupling genetic algorithm and CFD, Sci. China Technol. Sci. 59 (2016) 1475–1485, https://doi.org/10.1007/s11431-016-0373-x.

[26] M.V. Bozorg, M. Hossein Doranehgard, K. Hong, Q. Xiong, CFD study of heat transfer and fluid flow in a parabolic trough solar receiver with internal annular porous structure and synthetic oil–Al2O3 nanofluid, Renew. Energy. 145 (2020) 2598–2614, https://doi.org/10.1016/j.renene.2019.08.042.

[27] M. Siavashi, M. Vahabzadeh Bozorg, M.H. Toosi, A numerical analysis of the effects of nanofluid and porous media utilization on the performance of parabolic trough solar collectors, Sustain. Energy Technol. Assessments. 45 (2021), 101179, https://doi.org/10.1016/j.seta.2021.101179.

[28] Y. Aryan, M. Jannat Alipour, M. Siavashi, A.M. Norouzi, Heat transfer augmentation of a PTC with rotating absorber, utilizing nanofluid and porous lines, Sustain. Energy Technol. Assess. 52 (2022), 102229, https://doi.org/10.1016/j.seta.2022.102229.

[29] S. Samiezadeh, R. Khodaverdian, M.H. Doranehgard, H. Chehrmonavari, Q. Xiong, CFD simulation of thermal performance of hybrid oil-Cu-Al2O3 nanofluid flowing through the porous receiver tube inside a finned parabolic trough solar collector, Sustain. Energy Technol. Assess. 50 (2022), 101888, https://doi.org/10.1016/j.seta.2021.101888.

[30] N. Helmi, A. Nazari, M. Bezaatpour, S.K. Nateghi, H. Ghaebi, Investigation of energy storage in parabolic rotary trough solar collectors using various porous fins with magnetic nanoparticles, Energy Sustain. Dev. 70 (2022) 194–204, https://doi.org/10.1016/j.esd.2022.07.009.

[31] M.M. Heyhat, M. Zahi Khattar, On the effect of different placement schemes of metal foam as volumetric absorber on the thermal performance of a direct absorption parabolic trough solar collector, Energy (2022), 126428, https://doi.org/10.1016/j.energy.2022.126428.

[32] M.T. Jamal-Abad, S. Saedodin, M. Aminy, Experimental investigation on a solar parabolic trough collector for absorber tube filled with porous media, Renew. Energy. 107 (2017) 156–163, https://doi.org/10.1016/j.renene.2017.02.004.

[33] L. Suárez, Z. Wei, H. Teixidó, R. Sanjinés, M. Bensimon, C. Pulgarín, J. Kiwi, Cu-decorated Raschig-TiO2 rings inducing MB repetitive discoloration without release of Cu-ions under solar light, J. Environ. Chem. Eng. 5 (2017) 310–318, https://doi.org/10.1016/j.jece.2016.12.006.

[34] A. Salem, H. Afshin, H. Behsaz, Removal of lead by using Raschig rings manufactured with mixture of cement kiln dust, zeolite and bentonite, J. Hazard. Mater. 223–224 (2012) 13–23, https://doi.org/10.1016/j.jhazmat.2012.01.002.

[35] S.P. Rao, V. Gnielinski, Mass transfer in a packed bed of Raschig rings at low Peclet numbers, Lett. Heat Mass Transf. 7 (1980) 257–273, https://doi.org/10.1016/0094-4548(80)90011-9.

[36] S.A. Noseir, A. El-Kayar, H.A. Farag, G.H. Sedahmed, Forced convection solid - liquid mass transfer at a fixed bed of Raschig rings, Int. Commun. Heat Mass Transf. 22 (1995) 111–122, https://doi.org/10.1016/0735-1933(94)00057-R.

[37] A.H. El-Shazly, S.A. Nosier, M.Z. El-Abd, G.H. Sedahmed, Solid–liquid mass transfer at an oscillating packed bed of raschig rings, Ind. Eng. Chem. Res. 41 (2002) 5516–5522, https://doi.org/10.1021/ie020044b.

[38] M. Zaki, I. Nirdosh, G.H. Sedahmed, Natural convection mass transfer behaviour of vertical and horizontal cylinders embedded in an inert fixed bed of Raschig rings, Chem. Eng. Process. Process Intensif. 42 (2003) 977–984, https://doi.org/10.1016/S0255-2701(02)00138-1.

[39] P. Niegodajew, M. Marek, Statistical variation of characteristics of random packed beds of Raschig rings: The influence of the sample size, Particuology. 56 (2021) 50–61, https://doi.org/10.1016/j.partic.2020.11.004.

[40] S.K. Samantaray, S.S. Mohapatra, B. Munshi, Experimental findings and analysis of terminal velocity and drag coefficient of Raschig Ring in vertical and inclined channel, Powder Technol. 340 (2018) 440–448, https://doi.org/10.1016/j.powtec.2018.09.030.

[41] K. Tong, L. Yang, X. Du, Modelling of TiO2-based packing bed photocatalytic reactor with Raschig rings for phenol degradation by coupled CFD and DEM, Chem. Eng. J. 400 (2020), 125988, https://doi.org/10.1016/j.cej.2020.125988.

[42] M. Marek, Numerical simulation of a gas flow in a real geometry of random packed bed of Raschig rings, Chem. Eng. Sci. 161 (2017) 382–393, https://doi.org/10.1016/j.ces.2016.12.030.

[43] E.M. Moghaddam, E.A. Foumeny, A.I. Stankiewicz, J.T. Padding, Hydrodynamics of narrow-tube fixed bed reactors filled with Raschig rings, Chem. Eng. Sci. x. 5 (2020), 100057, https://doi.org/10.1016/j.cesx.2020.100057.

[44] E.M. Moghaddam, E.A. Foumeny, A.I. Stankiewicz, J.T. Padding, Heat transfer from wall to dense packing structures of spheres, cylinders and Raschig rings, Chem. Eng. J. 407 (2021), 127994, https://doi.org/10.1016/j.cej.2020.127994.

[45] H. Ebadi, A. Allio, A. Cammi, L. Savoldi, First numerical evaluation of the thermal performance of a tubular receiver equipped with Raschig rings for CSP applications. Power 2021, 2021, 10.1115/POWER2021-65714.

[46] B. Moyse, Raschig ring HDS catalysts reduce pressure drop, 82:53 (1984).

[47] A. Allio, R. Difonzo, A. Leggieri, F. Legrand, R. Marchesin, L. Savoldi, Test and Modeling of the Hydraulic Performance of High-Efficiency Cooling Configurations for Gyrotron Resonance Cavities, Energies. 13 (2020), https://doi.org/10.3390/en13051163.

[48] L. Savoldi, A. Allio, A. Bovento, M. Cantone, J. Fernandez Reche, Experimental and numerical investigation of a porous receiver equipped with Raschig Rings for CSP applications, Sol. Energy. (2020).

[49] H. Ebadi, A. Cammi, R. Difonzo, J. Rodríguez, L. Savoldi, Experimental investigation on an air tubular absorber enhanced with Raschig Rings porous medium in a solar furnace, Appl. Energy. 342 (2023), 121189.

[50] S. Salvi, A.P. Paranjape, Comparison of different types of Raschig rings, in, Third Int. Conf. Adv. Electr. Electron. Information, Commun. Bio-Informatics 2017 (2017) 56–60, https://doi.org/10.1109/AEEICB.2017.7972383.

[51] A. Boubault, C.K. Ho, A. Hall, T.N. Lambert, A. Ambrosini, Durability of solar absorber coatings and their cost-effectiveness, Sol. Energy Mater. Sol. Cells. 166 (2017) 176–184, https://doi.org/10.1016/j.solmat.2017.03.010.

[52] M. Cantone, M. Cagnoli, J. Fernandez Reche, L. Savoldi, One-side heating test and modeling of tubular receivers equipped with turbulence promoters for solar tower applications, Appl. Energy. 277 (2020), 115519, https://doi.org/10.1016/j.apenergy.2020.115519.

[53] J. Feng, M. Acton, E. Baglietto, A.R. Kraus, E. Merzari, On the relevance of turbulent structures resolution for cross-flow in a helical-coil tube bundle, Ann. Nucl. Energy. 140 (2020), 107298, https://doi.org/10.1016/j.anucene.2019.107298.

[54] L. Savoldi, K.A. Avramidis, F. Albajar, S. Alberti, A. Leggieri, F. Sanchez, A validation roadmap of multi-physics simulators of the resonator of MW-class CW gyrotrons for fusion applications, Energies. 14 (2021), https://doi.org/10.3390/en14238027.

[55] C.K. Ho, A.R. Mahoney, A. Ambrosini, M. Bencomo, A. Hall, T.N. Lambert, Characterization of Pyromark 2500 for High-Temperature Solar Receivers, (2012) 509–518. https://doi.org/10.1115/ES2012-91374.

[56] Effect of Input Parameter Uncertainty on Simulation Uncertainty, in: Stand. Verif. Cation Valid. Comput. Fluid Dyn. Heat Transf., ASME, 2009: pp. 1–26.

[57] B. Li, F.A.C. Oliveira, J. Rodríguez, J.C. Fernandes, L.G. Rosa, Numerical and experimental study on improving temperature uniformity of solar furnaces for materials processing, Sol. Energy. 115 (2015) 95–108, https://doi.org/10.1016/j.solener.2015.02.023.

[58] M.I. Roldán, R. Monterreal, Heat flux and temperature prediction on a volumetric receiver installed in a solar furnace, Appl. Energy. 120 (2014) 65–74, https://doi.org/10.1016/j.apenergy.2014.01.029.

[59] T. Wu, D. Wang, R. Wang, B. Zhao, M. Tang, S. Zhang, L. Nie, Pressure drop axial distribution uniformity of the particle bed in the radial bed, Korean J. Chem. Eng. 38 (2021) 1578–1591, https://doi.org/10.1007/s11814-021-0818-0.

[60] S. Das, N. Verma, M. Pathak, S. Bhattacharyya, Axially oriented structured porous layers for heat transfer enhancement in a solar receiver tube, J. Therm. Sci. 30 (2021) 1643–1657, https://doi.org/10.1007/s11630-021-1514-4.

[61] P. Wang, D.Y. Liu, C. Xu, Numerical study of heat transfer enhancement in the receiver tube of direct steam generation with parabolic trough by inserting metal foams, Appl. Energy. 102 (2013) 449–460, https://doi.org/10.1016/j.apenergy.2012.07.026.

[62] Z.-J. Zheng, M.-J. Li, Y.-L. He, Thermal analysis of solar central receiver tube with porous inserts and non-uniform heat flux, Appl. Energy. 185 (2017) 1152–1161, https://doi.org/10.1016/j.apenergy.2015.11.039.

[63] Y.C. Soo Too, R. Benito, Enhancing heat transfer in air tubular absorbers for concentrated solar thermal applications, Appl. Therm. Eng. 50 (2013) 1076–1083, https://doi.org/10.1016/j.applthermaleng.2012.06.025.